Investigation of mixing in gravity currents using high-resolution molecular tagging techniques

by

Tanmay Agrawal

ORCID: 0000-0002-0777-2527

A thesis submitted in total fulfillment for the
degree of Master of Philosophy

in the
Department of Mechanical Engineering
Melbourne School of Engineering
THE UNIVERSITY OF MELBOURNE

February 2021

THE UNIVERSITY OF MELBOURNE

Abstract

Gravity currents are horizontal flows of fluid of a higher density into an ambient fluid of slightly lower density. They occur frequently in the atmosphere as sea-breeze fronts, thunderstorm outflows, katabatic flows etc., and are also encountered in industrial applications. The initial density difference between the two fluids can either be due to the presence of a salt or a temperature difference. While a majority of the studies employ a salinity based stratification, this work focuses on the flow dynamics of a gravity current generated as a result of an initial temperature difference.

In the laboratory environment, a gravity current can be produced using a lock-exchange experiment in which the two fluids, initially at rest, are separated by a vertical barrier (or lock gate). At time $t = 0$, a rapid removal of the lock gate results in the formation of a gravity current. The present gravity currents were produced in a Perspex tank of 2.0 m x 0.2 m x 0.2 m where the lock was located mid-way. The present flows were first visualized by mixing a dye in the heavier (cold) side to evaluate the bulk properties of the flow e.g. Froude number, Fr. Subsequently, simultaneous measurements of streamwise velocity and temperature field were conducted using the single-component molecular tagging velocimetry (1c-MTV) and molecular tagging thermometry (MTT) respectively. These experiments were focused at the interface between the hot and cold fluid to estimate the resultant mixing across the interface. The measurements were acquired using a 1024 x 1024 pixel Princeton Instruments PI: MAX4 camera and were shown to resolve the Kolmogorov (velocity) and Batchelor (scalar) length scales. To the author's knowledge, to date no previous experimental study has documented lock-exchange mixing at this level of resolution.

The obtained density (temperature) distribution allows an estimation of the background potential energy of the flow which was used to quantify the diapycnal mixing. Specifically, mixing is attributed to the irreversible changes in fluid properties associated with fluid motions [1] and therefore differentiated from buoyancy induced reversible stirring. These measurements yield a mixing efficiency of 0.13 for the Reynolds number range considered ($Re \leq \mathcal{O}(10^4)$). Flow analysis revealed that the locally high values of mixing efficiency occur *after* the occurrence of certain dissipative stirring events in the flow. These events, largely associated with vortical overturns, are commonly observed at the interface between the two fluids and are shown to lead the locally efficient mixing.

Declaration of Authorship

I, TANMAY AGRAWAL, declare that this thesis titled, 'INVESTIGATION OF MIXING IN GRAVITY CURRENTS USING HIGH-RESOLUTION MOLECULAR TAGGING TECHNIQUES' and the work presented in it are my own. I confirm that:

- The thesis comprises only my original work towards the MASTER OF PHILOSOPHY except where indicated in the preface;
- due acknowledgement has been made in the text to all other material used; and
- the thesis is fewer than the maximum word limit in length, exclusive of tables, maps, bibliographies and appendices as approved by the Research Higher Degrees Committee.

Signed:
TANMAY AGRAWAL

Date:
September 21, 2020

Acknowledgements

While it might be true that the front page of this thesis bears only my name, however, this work would not be possible without an active involvement of many people without thanking whom I might not justify the content of this thesis.

First and foremost, I would like to express my most sincerest gratitude to my supervisors, Prof. Joe Klewicki and Dr. Jimmy Philip, whose constant guidance and support have been proven extremely valuable during my candidature. Their research experience and expertise has helped me immensely to build a foundation in the field of experimental fluid dynamics, an area I knew almost negligibly before I was admitted to the University of Melbourne. To be brutally honest, I couldn't achieve even a fraction of the work that I am presenting here without their continuous motivation and curiosity. Therefore, I consider myself very fortunate to have had this opportunity to learn from them. I would also like to acknowledge Joe's assistant, Ms. Emma Mitchell, for scheduling (and rescheduling) my supervision meetings and providing help on multiple occasions.

My first collaboration in the hydrodynamics lab was with Dr. John Elsnab who was later, also my committee member. Through his expertise in MTV, I was able to learn some of the things that helped me throughout the time I spent therein. He has been my on-the-field mentor, a go-to personnel during the times I messed things up and therefore, I'll always be grateful for that. I'd also thank my committee chair Prof. Jason Monty for all the valuable feedback he provided during my review meetings and to ensure that the hydro lab provides a great ambiance for people like me to work in.

I would also like to thank my friends and colleagues in the fluid mechanics group. Special thanks to Dr. Spencer Zimmerman who was actively involved not only during the fabrication of lock-exchange facility, but also in the later half of my candidature providing many useful pointers towards this thesis. During this ongoing *coronavirus* crisis, I am thankful to Dr. Will Junghoon Lee for prioritizing me to use the research spaces. In the moments of ups and downs, I am extremely grateful for the time and family-like comfort provided to me by the Indian community.

Finally, I would take this time to thank my family who trusted me all the way up to here. Being physically miles apart and supporting my ambitions without a second thought, their love and compassion has shaped not only this thesis, but also my personality.

Contents

List of Figures

List of Tables

Symbols

u	Instantaneous streamwise velocity
v	Instantaneous spanwise velocity
w	Instantaneous vertical velocity
U	Mean streamwise velocity
g	Acceleration due to gravity
h	Flow depth
H	Total depth
p	Pressure
ρ	Density
ν	Kinematic viscosity
E_P	Potential energy
κ	Thermal diffusivity
E_K	Kinetic energy
ϵ	Rate of dissipation
g	Acceleration due to gravity
$\mathcal{P}_B$	Background potential energy
ρ_0	Reference density
$\mathcal{M}$	Instantaneous mixing rate
ϕ_d	Diapycnal mixing
ϕ_z	Buoyancy flux
R_f	Richardson number
ε_i	Instantaneous mixing efficiency
ε_c	Cumulative mixing efficiency
λ_K	Kolmogorov length scale
λ_B	Batchelor length scale

Sc	Schmidt number
Re	Reynolds number
Fr	Froude number
S_1	Phosphorescence intensity (undeformed)
S_2	Phosphorescence intensity (deformed)
τ	Phosphorescence lifetime
t	Time

Chapter 1

Introduction

Gravity currents are horizontal flows of fluid of one density into an ambient fluid of slightly different density. A buoyancy force manifests and drives the flow as a result of density difference between the two fluids. A simple example is the current that flows into a warm house through an open doorway on a cold, windless day. The cold heavier air that resides outside the doorway provides a higher pressure than that of the warm lighter one on the inside. This pressure difference drives the cold air along the bottom while the warm air flow through the top of doorway [10].

Some other examples of gravity currents are shown in figure 1.1. An atmospheric gravity current, called *Haboob*, Arabic for 'strong wind' is depicted in figure 1.1a. A haboob is formed when the cold air generated by a thunderstorm spreads out along the surface of the earth and could be as high as 1500 m. On the other hand, figure 1.1b presents the case of an accidental release of a dense gas. These incidents are encountered in industries where the gases can be flammable or toxic. Another commonly occurring gravity current in nature (not shown here), is a sea-breeze front. These are formed when, during the day time, the warm air produced by a coastal land migrates towards the sea with a simultaneous inland motion of cold sea air. During the night time, however, the flow direction reverses. These fronts can transport local climatic conditions as well as pollutants inland.

The first attempt to quantify these currents was made by von Kármán in 1940 when he was asked by the American military to evaluate under what wind conditions would a poisonous gas propagate forward to envelop the enemy, rather than drifting backwards

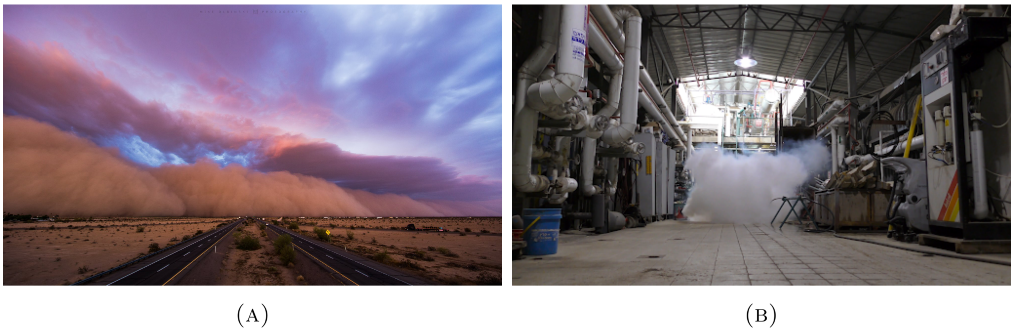

(A)

(B)

Figure 1.1: (A) The front of a *Haboob* over Arizona in United States (Source: Washington Post). (B) An example of accidental gas leakage in a factory (Source: Success Link Community)

to create havoc among those who released the gas [11]. To understand this, he considered an infinitely deep ambient fluid layer of density, ρ_1, and a current of density $\rho_2 > \rho_1$. Assuming irrotationality of a perfect fluid, and by using Bernoulli's equation, he deduced that the speed of the current may be expressed in a non-dimensional form as

$$F_h \equiv \frac{U}{\sqrt{g(1-\gamma)h}} = \sqrt{\frac{2}{\gamma}}. \tag{1.1}$$

where U is the speed of the current, $\gamma = \frac{\rho_1}{\rho_2}$ is the density ratio, such that $0 < \gamma < 1$ and h refers to the height of the current. For a Boussinesq flow, $\gamma \approx 1$, and defining the reduced gravity, g' as $g' = g(1-\gamma)$, (1.1) reduces to the celebrated result for the front Froude number of a Bousinnesq current in a deep ambient fluid

$$F_h = \frac{U}{\sqrt{g\prime h}} = \sqrt{2}. \tag{1.2}$$

This result indicates that the Froude number assumes a constant value but fails to provide a direct estimate of the propagation speed, U, or the associated height, h. Unfortunately, this framework lacked another independent equation to solve for either of these important characteristics of the flow.

This problem was eventually addressed in detail almost three decades later when Benjamin [1] proposed a theory for the flow of inviscid gravity currents. Benjamin introduced a two-layer model for understanding the dynamics of such currents using an integral approach based on momentum flux conservation across the head of the current. Despite the inherent simplifications involved in this approach, the results of Benjamin's work capture the primary dynamics of gravity currents. This approach and the associated dynamics are now described.

1.1 Theory of inviscid gravity currents

Benjamin [1] considered a two-dimensional gravity current flowing along the bottom boundary in a rectangular channel as shown in figure 1.2. He assumed that the far upstream and downstream ends of the front were hydrostatic and that there was no relative motion within the current. Therefore, the whole current moves as a slug without any internal flow relative to the advancing front. The theoretical analysis of the current is now presented in brief and can be found in a greater detail in Linden [10]. Continuing with the previous notation, we consider ρ_1 and ρ_2 to be the densities of ambient and heavy fluids respectively and the current advancing with a constant and uniform velocity U and depth h.

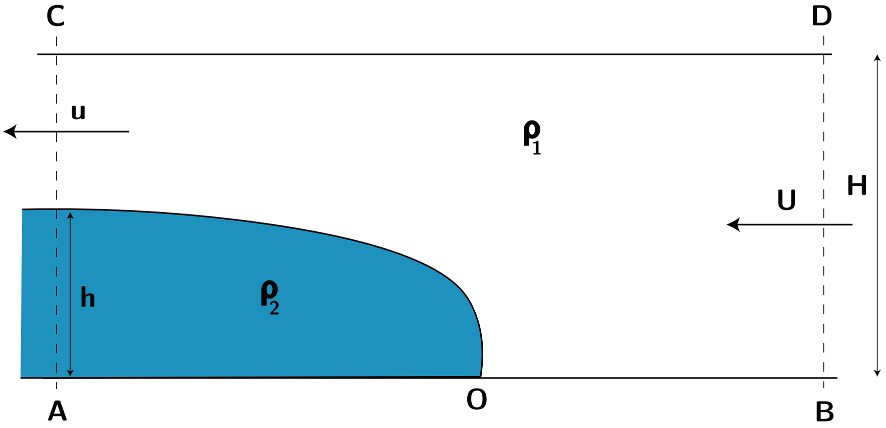

FIGURE 1.2: Schematic of the energy-conserving current as studied by Benjamin [1]. Blue region corresponds to heavy fluid and the reference frame is selected to move with the front.

Applying the continuity equation in a reference frame moving with the front yields:

$$UH = u\,(H - h). \tag{1.3}$$

(1.3) essentially derives from consideration of the control volume ABCD in figure 1.2. As previously mentioned, the velocities within the current are neglected in this equation. Next, since there are no external horizontal forces acting on the flow, the net flux of horizontal momentum into the control volume, $ACDB$, is zero. Mathematically, this can be written as:

$$\int_A^C p dz + \int_A^C \rho u^2 dz = \int_B^D p dz + \int_B^D \rho U^2 dz. \tag{1.4}$$

The pressure distribution along the two edges of control volume may be determined since the flow is assumed hydrostatic. Along AC, we can write:

$$p = \begin{cases} p_A - g\rho_2 z, & \text{if } 0 < z < h \\ p_A - g\rho_2 h - g\rho_1 (z-h) & \text{if } h < z < H \end{cases} \tag{1.5}$$

where p_A is the pressure at point A. Similarly along BD, we can write:

$$p = p_B - g\rho_1 z \tag{1.6}$$

where p_B is the pressure at B.

Now, if we define the pressure at the stagnation point O to be p_O, the application of Bernoulli's equation along AO gives $p_A = p_O$, since the velocity within the current is zero. Similarly, along OB, we can write $p_B = p_O - \frac{1}{2}\rho_1 U^2$. Therefore, substitution of (1.5) and (1.6) into the momentum balance (1.4) and using continuity (1.3) gives:

$$\frac{U^2}{gH} = \frac{1-\gamma}{\gamma}\left(\frac{h(2H-h)(H-h)}{H^2(H+h)}\right). \tag{1.7}$$

(1.7) forms one of the two equations needed to determine the properties of the current. In order to completely determine the flow, an additional condition is needed to specify h. Benjamin [1] further assumed that there is no dissipation in the flow and applying the Bernoulli equation either along the upper boundary of the channel or along the interface between the two fluids results in

$$\frac{U^2}{gH} = 2\frac{1-\gamma}{\gamma}\left(\frac{h(H-h)^2}{H^3}\right). \tag{1.8}$$

Equating (1.7) and (1.8) gives two solutions for the current depth

$$\frac{h}{H} = 0 \quad \text{or} \quad \frac{h}{H} = \frac{1}{2}. \tag{1.9}$$

Therefore, *energy conserving* currents either have zero depth at the front or they occupy half the full depth of the domain they are propagating in. While a current with zero depth is not physically possible, most of the experimental and numerical observations till date follow (1.9) as in they occupy almost half the total height of the domain [12–16] validating this result. Benjamin further postulated that currents occupying less than half the depth were dissipative in nature and that external energy is required to sustain the currents greater than half the domain depth.

Assuming the Boussinesq approximation (i.e., $\gamma \approx 1$), and substituting (1.9) into (1.7) or (1.8) shows that,

$$\frac{U}{\sqrt{g'H}} = \frac{1}{2}. \tag{1.10}$$

In fact, the above equation was first derived by Yih [17] using a simpler energy argument. In the present work (to be described in detail later), we use a channel with a centrally-located lock, that yeilds conditions satisfying (1.10). Finally, notice that both (1.7) and (1.8) in the limit of large h/H (i.e., gravity current in an infinite fluid extent) recovers the expression (1.2) derived by von Kármán.

1.2 A lock-exchange experiment

There are many ways to obtain a gravity current in the laboratory. A common technique employed by many researchers is called as a lock-exchange or a lock-release experiment [6, 15, 18–21]. In this experiment, a finite volume of dense homogeneous fluid is released into another homogeneous fluid of slightly different density. These fluids are initially separated by a vertical barrier, the lock gate as shown in figure 1.3. Here we represent the density of heavier fluid as ρ_C, where the subscript C symbolizes a cold fluid while the density of ambient fluid is represented as ρ_H, the subscript H symbolizes hot. These notations essentially capture the initial thermal state of fluid. In the present work, as described in detail later, the desired density difference between the two fluids is obtained by maintaining the two fluids at different temperatures.

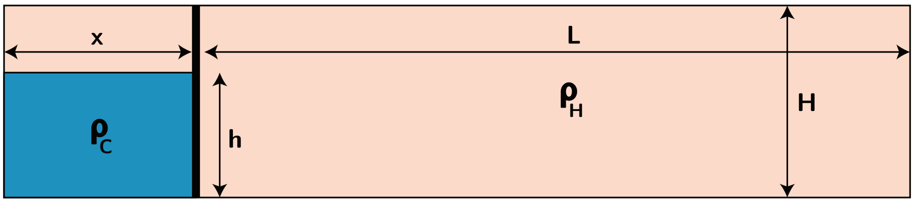

FIGURE 1.3: Schematic of a general lock-exchange experiment. Blue color corresponds to heavy (cold) fluid while the pink color represents light (hot) fluid. Lock gate is represented as a vertical dark line.

Geometrically, four variations of lock-exchange experiments are possible as detailed below:

- $h < H$ and $x < L$: In this configuration, the dense fluid occupies a fraction of the total depth of the tank, thereby being referred as *partial-depth*. Also, the horizontal extent of the dense fluid is smaller than that of the ambient fluid, and therefore referred to as a *partial-lock* exchange. To achieve equal fluid levels on either side of the lock prior to experiment, lighter fluid is filled on top of the dense fluid as shown in figure 1.3.

- $h < H$ and $x = L$: This configuration consists of equal horizontal extents of the two fluids. This prevents transitions in the flow associated with end-wall reflection which occur in partial-lock configurations. In particular, for partial-lock configurations, the lighter gravity current hits the end-wall producing a bore like structure in the heavier current that eventually overtakes the heavier current head altering its dynamics.

- $h = H$ and $x < L$: This is one of the widely studied configurations in which the tank is filled to the same height on both sides of the lock with the volume of dense fluid being a fraction of the total tank volume. This configuration allows studying the different stages of the gravity current produced. Since the height of the two fluids are identical at the start of experiment, this case is referred to as a *full-depth* experiment.

- $h = H$ and $x = L$: This is the configuration used for the present experiments. Here, before the experiment commences, the heights as well as the volumes of the two fluids are identical. This configuration with the usual experimental limitations of the channel length, as detailed later, restricts the current to its slumping phase, i.e. here the propagation speed of the current is approximately constant. We, however, do satisfy a constant Froude number condition of (1.10). Interestingly, in the slumping phase apart from the current velocity (U), the height (h) is also approximately constant, which is unlike the self-similar phase (detailed in the next chapter) where both U and h decreases with time. The constant U turns out to be a better condition for averaging purposes when we investigate the 'mixing efficiency' that would form bulk of this thesis.

1.2.1 Governing equations

For the case of Boussinesq approximated buoyancy driven flows, the governing conservation equations can be written in dimensional form as:

$$\frac{Du_i}{Dt} = -\frac{1}{\rho_0}\frac{\partial p}{\partial x_i} - \frac{g}{\rho_0}\rho\delta_{i3} + \nu\frac{\partial^2 u_i}{\partial x_j^2}, \tag{1.11}$$

$$\frac{\partial u_i}{\partial x_i} = 0, \tag{1.12}$$

$$\frac{D\rho}{Dt} = \kappa\frac{\partial^2 \rho}{\partial x_j^2}. \tag{1.13}$$

Herein, the repeated indices imply summation ($i, j = 1, 2, 3$). The gravitational acceleration is directed downwards vertically, $x_3 = z$. The velocity field is represented by u whereas p denotes the pressure. ρ and ν are the density and kinematic viscosity of the fluid. ρ_0 is a constant reference density and κ is the thermal diffusivity of the fluid. Physically, (1.11), (1.12) and (1.13) represent the conservation of momentum, volume and internal energy respectively. In writing these equations, the thermal expansion of the fluid and dissipation due to shear viscosity are ignored. Further, a linear relationship between temperature and density is assumed.

1.2.1.1 Potential energy

For a general flow, the total potential energy can simply be written as:

$$E_P = g\int_V \rho z dV, \tag{1.14}$$

where, z is the vertical direction (positive upwards). For a lock-exchange flow, the initial energy of the system that drives the flow is stored in the form of this potential energy. To understand how it changes during an experiment, one can write the time evolution of (1.14) as [22]:

$$\frac{d}{dt}E_P = g\int_V \left(\rho\frac{dz}{dt} + z\frac{\partial\rho}{\partial t}\right) dV, \tag{1.15}$$

where the volume considered remains fixed in time. To simplify this equation, we now employ the energy equation, (1.13). Expanding this yields

$$\frac{\partial \rho}{\partial t} + u_j \frac{\partial \rho}{\partial x_j} = \kappa \frac{\partial^2 \rho}{\partial x_j^2}, \tag{1.16}$$

and invoking (1.15) results in

$$\frac{d}{dt} E_P = g \int_V \left(\rho w + z \left(\kappa \frac{\partial^2 \rho}{\partial x_j^2} - u_j \frac{\partial \rho}{\partial x_j} \right) \right) dV, \tag{1.17}$$

where w is the vertical velocity. The second and third terms inside the integral in (1.17) can be modified using the vector identity $\nabla \cdot (s\mathbf{A}) = s\nabla \cdot \mathbf{A} + \mathbf{A} \cdot \nabla s$ for any scalar s. Specifically, the second term inside the integral can be simplified after using the divergence theorem as

$$\int_V g\,\kappa\,z \frac{\partial^2 \rho}{\partial x_j^2} dV = \oint_S g\,\kappa\,z\,\boldsymbol{\nabla \rho} \boldsymbol{\cdot} \boldsymbol{n} dS - \kappa\,g\,A\,(\overline{\rho_T} - \overline{\rho_B}),$$

where $\overline{\rho_T}$ and $\overline{\rho_B}$ are average densities at the top and bottom planes, associated with the area S. Similarly, the third term in (1.17) can be simplified by using the continuity equation (1.12) as

$$\int_V g z u_j \frac{\partial \rho}{\partial x_j} dV = \oint_S g z \rho \boldsymbol{u} \boldsymbol{\cdot} \boldsymbol{n} dS.$$

With these manipulations, one can write the evolution equation for the total potential energy as

$$\frac{d}{dt} E_P = - \oint_S g z \rho \boldsymbol{u} \boldsymbol{\cdot} \boldsymbol{n} dS + \int_V g \rho w dV + \oint_S g \kappa z \boldsymbol{\nabla \rho} \boldsymbol{\cdot} \boldsymbol{n} dS - \kappa g A(\overline{\rho_T} - \overline{\rho_B}). \tag{1.18}$$

Physically, the first and the third terms respectively represent the advective and diffusive fluxes across the bounding surface S. For a closed system, these terms are zero. The second term represents the reversible buoyancy flux (which is later denoted later as ϕ_z, and plays a crucial role in stratified flows). The fourth term is the Boussinesq form of the conversion rate from internal to potential energy [22–24]. Here, the overbars represent an averaging along the horizontal surfaces of the bounding control volume.

1.2.1.2 Kinetic energy

The kinetic energy, E_k, of a general flow field is defined as

$$E_k = \frac{\rho_0}{2}\int_V (u^2+v^2+w^2)\ dV \tag{1.19}$$

Employing the momentum equation, (1.11), the rate of change of E_k within the control volume, V, can be written as [22, 25]

$$\frac{dE_k}{dt} = -\int_V \left(p\partial_i u_i + \rho_0\partial_i u_j \frac{1}{2}(u^2+v^2+w^2) - \frac{\partial u_i}{\partial x_j}\tau_{ij} - g\rho w\right) dV - \epsilon \tag{1.20}$$

Here, τ_{ij} represents the shear stress and $\epsilon = 2\nu S_i j S_i j$ is the volumetrically averaged dissipation rate and $S_i j$ represents the strain rate. The term represented as $\int_V g\rho w dV$ is the buoyancy flux (ϕ_z) and quantifies the conversion of kinetic energy into potential energy. The interactions between E_k and other energy forms are discussed later.

1.2.1.3 Background potential energy

The concept of background potential energy was first formally introduced by Lorenz [26] in concert with the introduction of available potential energy. Essentially, he decomposed the total potential energy of a flow into two states: the background potential energy and an available potential energy. Fundamentally, the background potential energy (BPE) of a system is defined as the state of minimum potential energy [22]. This is achieved by adiabatically redistributing or ‘sorting’ the three-dimensional density field into a monotonically increasing vertical profile i.e. a background density profile $\rho_*(z,t)$. Referring to this as a background state, the BPE, $\mathcal{P}_B$, may be expressed as

$$\mathcal{P}_B = \frac{g}{\rho_0}\int_V \rho_*(z,t)\ z, \tag{1.21}$$

Here, $\mathcal{P}_B$ denotes the averaged BPE per unit mass and is therefore normalized by ρ_0.

One can study the evolution of BPE by taking a time-derivative of (1.21). This time-evolution can be expressed as (referring to Winters et al. [22] and Salehipour and Peltier [24] for a complete derivation)

$$\frac{d}{dt}\mathcal{P}_B = \frac{g}{\rho_0 V}\int_V z_*(-\mathbf{u}\cdot\nabla\rho + \kappa\nabla^2\rho)dV. \tag{1.22}$$

In (1.22), z_* is the vertical position in the reference state of minimum potential energy. Employing integration by parts to the terms inside the volume integral, one can write the final form of evolution equation of BPE as

$$\frac{d}{dt}\mathcal{P}_B = \left(-\frac{g}{\rho_0 V}\oint_S \psi \mathbf{u}\cdot n \, dS + \kappa \oint_S z_* \nabla\rho \cdot n \, dS + \underbrace{\kappa \int_V -\frac{dz_*}{d\rho}|\nabla\rho|^2 \, dV}_{\phi_d} \right). \tag{1.23}$$

Here, $\psi = \int z_* \, d\rho$ incorporates the implicit dependence of z_* on ρ. Physically, the first and second terms respectively represent the rate of change of background potential energy due to advective and diffusive flux transfers across the surface S. These terms are zero for a closed system. The third term, denoted as ϕ_d in Winters et al. [22], provides the rate of change of $\mathcal{P}_B$ due to material changes in density within the control volume, or equivalently, due to the diapycnal mixing. Peltier and Caulfield [23] demonstrated that there are two contributing factors towards ϕ_d:

1. Diffusion as a result of the conversion of internal energy of the fluid to its potential energy, written mathematically as $\phi_i = -\kappa g A(\overline{\rho_T} - \overline{\rho_B})$. Note that this term also appears in (1.18).
2. The rate of mixing associated with macroscopic fluid motion, $\mathcal{M} = \phi_d - \phi_i$ as a result of *irreversible* changes in the density field. Physically, $\mathcal{M}$ represents the small-scale diffusive phenomenons those result in permanent changes in the flow properties e.g. density. It would be detailed further in the next section.

Generally, for turbulent flows, the magnitude of ϕ_i is much smaller than that of $\mathcal{M}$ [24], and therefore one can use the approximation

$$\mathcal{M} \approx \frac{\kappa g}{\rho_0 V}\int_V -\left(\frac{d\rho_*}{dz}\right)^{-1} |\nabla\rho|^2 \, dV. \tag{1.24}$$

These processes of energy conversion, referred to as the *energetics* of stratified flows, are depicted in figure 1.4 [22, 23]. Double-sided arrows correspond to reversible exchange processes whereas a single-sided arrow represents an irreversible phenomenon.

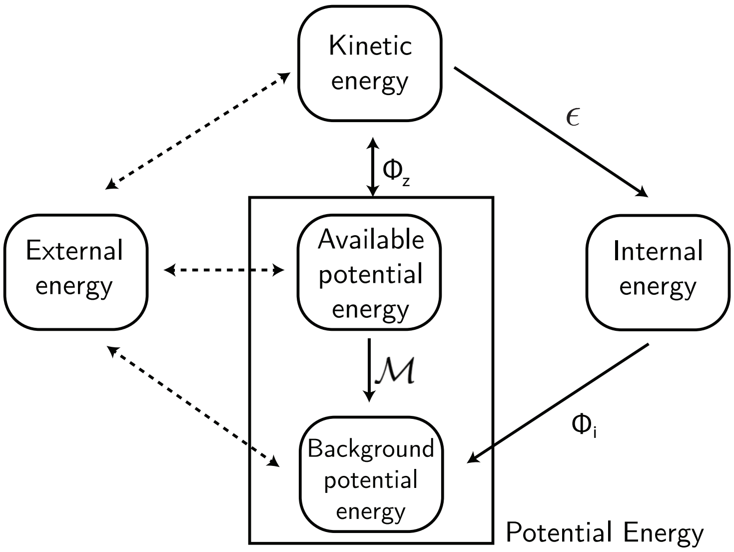

FIGURE 1.4: Energy diagram for a density stratified Boussinesq flow. The dashed arrows represent surface fluxes for an open system. ϵ represents viscous dissipation.

1.3 Mixing in stratified flows

The primary objective of this section is to distinguish between the physical processes of 'stirring' and 'mixing' in the context of stratified flows. From an energy viewpoint, stirring is a *reversible* exchange of energy between the kinetic and potential energy reservoirs. On the other hand, the phenomenon of mixing results in an *irreversible* change in fluid properties. Consider, for example, the upward motion of an anomalously dense fluid parcel by the flow that leads to an increase in the available potential energy of the system. This increment occurs through an exchange with the kinetic energy reservoir via the buoyancy flux ϕ_z (see (1.20) and figure 1.4). There are subsequently two pathways for this increased potential energy to decay. In first scenario, the diffusion could act on sufficiently small scales and change the density of the lifted dense fluid parcel and its neighbours. This process is referred to as mixing. The other choice for the lifted parcel is to fall back under gravity, reconverting the temporarily stored potential energy into kinetic energy. This non-diffusive process of stirring does not result in a permanent change in fluid properties.

An important parameter to quantify mixing in stratified flows is the mixing efficiency. Mathematically, researchers have expressed mixing efficiency in many different ways. [27]. Osborn [28] considered the case of a statistically stationary and homogeneous turbulent flow and provided a measure of mixing efficiency in the form of Richardson number

$$R_f = \frac{\phi_z}{P}, \tag{1.25}$$

where ϕ_z is the buoyancy flux and $P = \overline{u_i' u_j'} \frac{\partial \overline{u_i}}{\partial x_j}$ is the rate of production of turbulent kinetic energy, k. The term $\Gamma = R_f/(1 - R_f)$ was identified as mixing efficiency in his work. Based on experimental observations and theoretical predictions, Osborn recommended a canonical value of $R_f \approx 0.17$ (i.e. $\Gamma \approx 0.2$). Despite the fact that this definition was able to provide *reasonable* estimates of mixing efficiency in certain situations, there is a lack of universal parameterization of the mixing efficiency due to overall complexity of stratified flows.

A decade or so later, to remedy for the inherent assumptions of stationarity and homogeneity in Osborn's work, Ivey and Imberger [29] proposed an alternate general definition of mixing efficiency as:

$$\hat{R_f} = \frac{\phi_z}{\phi_z + \epsilon}. \tag{1.26}$$

Here, ϵ as defined previously, is the dissipation rate of k. For stationary homogeneous shear flows, (1.26) is identical to (1.25). While this definition considers the inhomogeneity and time-variability of a flow field, it inherently assumes that all the contribution from the buoyancy flux, ϕ_z, results in 'mixing' whereas in stratified flows, a (significant) fraction of ϕ_z could simply result in reversible 'stirring' as described earlier. In other words, this definition suffers from the effects of countergradient fluxes that are commonly observed in strongly stratified flows.

Therefore, a third definition of mixing efficiency was introduced by Peltier and Caulfield [23], that accounts for *only* the irreversible components of the buoyancy fluxes towards mixing, caused by 'macroscopic' fluid motion resulting in an increase in the background potential energy. Note that ϕ_i also contributes to the mixing by 'microscopic' processes. They proposed

$$\varepsilon_i = \frac{\mathcal{M}}{\mathcal{M} + \epsilon}. \tag{1.27}$$

Here, $\mathcal{M}$ is the irreversible contribution to buoyancy flux through an exchange with the available potential energy (refer to figure 1.4). For stationary homogeneous flows, the three definitions are equivalent. However, such conditions are a rare occurrence in stratified flows. Peltier and Caulfield [23] termed (1.27) as an *instantaneous* mixing efficiency and provided the following definition to account for the time-variability of a general flow field:

$$\varepsilon_c = \frac{\int_0^T \mathcal{M} dt}{\int_0^T \mathcal{M} dt + \int_0^T \epsilon dt}. \tag{1.28}$$

1.4 Research questions to address

As detailed in the next chapter, there has been a significant amount of research to understand the dynamics of gravity currents generated through a lock-exchange experiment. However, in a majority of such studies, the required stratification was generated by dissolving a salt [6, 12, 21, 30–34]. To the best of the present author's knowledge, there has not been much emphasis on the mixing efficiency when a thermal stratification drives the flow. To address these, we introduce a temperature inhomogeneity across the lock and study the resulting gravity current.

The characteristic length scales associated with stratified turbulent flows are the Kolmogorov (λ_K) and Batchelor (λ_B) scales for the velocity and scalar fields respectively. Mathematically, these are given as:

$$\lambda_K = \left(\frac{\nu^3}{\epsilon}\right)^{\frac{1}{4}} \quad \text{and} \quad \lambda_B = \frac{\lambda_K}{\sqrt{Sc}}, \tag{1.29}$$

where ν is the molecular diffusivity and $Sc = \nu/\kappa$ is the Schmidt number. Physically, they correspond to the smallest length scales at which the velocity/scalar field dissipates. From (1.29), $Sc > 1$ implies that the λ_B is smaller than λ_K, which happens to be the case with most fluids. In the context of stratified flows, dissolving a salt in water results in $Sc \sim 700$. Whereas for a thermal stratification, Sc is equivalent to the Prandtl number, Pr, of the fluid and therefore, $Sc \sim 7$. Essentially, it implies that the scalar dissipates at relatively larger scale in a thermally stratified flow as compared to its saline counterpart. From an experimental perspective, resolving these length scales is a very challenging task. It is quite common to resolve the Batchelor scale for temperature at a 'point'. But it is quite rare to find a study that will resolve temperature along a 'line'. This line information is needed for estimating $\mathcal{P}_B$ and the mixing efficiency, which has so far been limited to only DNS. As discussed in detail later, the present measurement technique offers high spatial resolution, and therefore offer capabilities to resolve fine scales in a lock-exchange experiment.

Specifically, in this thesis we will try to provide answers to the following problems:

- How suitable are the molecular tagging techniques, described in sections 2.1.1 and 2.1.2, in measuring simultaneous velocity and temperature in a full-depth lock-exchange flow? What are the uncertainties associated with these velocity and temperature fields?
- How does the spatial resolution of the employed technique compare against the characteristic length scales of these flows?
- Can these measurements be used to quantify mixing? If (1.27) and (1.28) are employed to calculate the mixing efficiency, how does it compare against the results of other studies?
- Lastly, we focus on the physical understanding of instantaneous mixing efficiency (1.27). For a lock-exchange flow that exhibits time-variability, we will try to find a relation between the instantaneous mixing efficiency and certain instabilities or events in the flow.

In this regard, the broad outline of this thesis is as follows. Chapter 2 presents the relevant definitions and background work including the details and working principle of the measurement technique. The flow physics of a lock-exchange experiment with a special emphasis on mixing is also discussed. Chapter 3 provides a detailed description of various experiments that have been conducted in order to probe the flow field. Chapter 4 contains the general findings of this research. It attempts to answer the aforementioned questions. Finally, chapter 5 concludes the present work and suggests possible future directions.

Chapter 2

Literature Survey

This chapter presents the relevant literature review and is divided into two parts. The first section emphasises the measurement techniques. In this study, we are using a subset of molecular tagging techniques referred to as molecular tagging velocimetry and molecular tagging thermometry to measure velocity and temperature fields respectively. In this section, we detail the working principles of these techniques along with the notable studies that have employed and advanced their usage. The flow physics of lock-exchange flow is subsequently addressed in second part of this chapter. Herein, we describe the different phases of flow evolution that are observed in this flow. Finally, we close this chapter with a discussion pertaining to mixing in such flows. Specifically, previous full-depth lock-exchange flow studies that have either qualitatively or quantitatively analyzed mixing and mixing efficiency are discussed.

2.1 Measurement technique

2.1.1 Molecular Tagging Velocimetry

Molecular Tagging Velocimetry (MTV) is a whole field optical technique used to measure one or more components of velocity in a fluid flow. It takes advantage of the photoluminescence properties of certain molecules that are either naturally present in the flow or premixed with the flowing medium. The photoluminescence phenomena of fluorescence and phosphorescence refer to the radiative processes through which a molecule transitions from an excited state to its ground state. In fluorescence, this transition happens from a singlet excited state to a singlet ground state. Such singlet-singlet transitions are quantum mechanically allowed, therefore they are highly probabilistic making fluorescence short lived with an emission lifetime of the order of nanoseconds. On the other hand, phosphorescence involves the molecule transition from a triplet excited state to its ground state. Such an exchange being quantum mechanically forbidden results in a phosphorescence lifetime of the order of microseconds or even minutes in some cases [3, 35]. A molecular complex is deemed suitable for MTV applications if its lifetime as a tracer is long enough compared to the flow convection time scale. This allows sufficient macroscopic displacement of the tagged regions during the interrogation time frame. In a number of respects, this technique can be thought of as a molecular counterpart of Particle Image Velocimetry (PIV) where the analogous "seeding particles" are dissolved in the flowing medium on a microscopic level. This eliminates problems that could be associated with actual particle seeding.

As described in greater detail in Koochesfahani and Nocera [3], there are four distinct mechanisms that encompass the current MTV techniques.

1. MTV by absorbance, e.g. Laser Induced Photochemical Anemometry (LIPA),
2. MTV by Vibrational Excited State Fluorescence, e.g. Raman Excitation plus Laser-Induced Electronic Fluorescence (RELIEF),
3. MTV by Photoproduct Fluorescence, e.g. PHoto-Activated Nonintrusive Tracking Of Molecular Motion (PHANTOMM), Hydroxyl Tagging Velocimetry (HTV) and Ozone Tagging Velocimetry (OTV) and
4. MTV by Direct Phosphorescence.

The present experiments employ the direct phosphorescence technique. A single light source is needed to obtain the luminescent excited state that, in a relative sense, is extremely long-lived. Once decayed to its ground state, the molecule can be excited again making it re-usable, i.e. the process is reversible. The overarching approach of using MTV through this technique has similarities to Laser Induced Fluorescence (LIF).

For the measurements presented in this thesis, a phosphorescent *supramolecule*, initially designed by Ponce et al. [36] and subsequently improved by Hartmann et al. [37], is employed. This molecular design comprises a lumophore (light emitting molecule) that

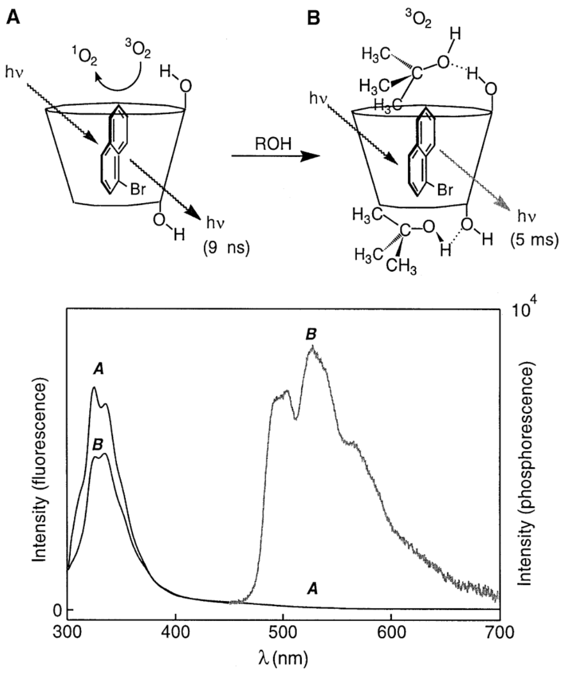

Figure 2.1: Photoluminescence properties of 1-BrNp in CDs in the absence (A) and presence (B) of an appropriate alcohol (ROH). An additional bright green phosphorescence is observed in the latter case. Adopted from Gendrich et al. [2]

.

is protected from oxygen and water *quenching* by mixing certain alcohols (represented as ROH) and an aqueous solution of a cyclodextrin (CD). These individual units combine in such a way that the lumophore is contained in the cyclodextrin 'cup' while an ROH 'lid' aids towards suppressing quenching (see figure 2.1 B). Cyclodextrins that have been used in most of the MTV measurements to date are either Gβ-CD or Mβ-CD while the lumophore being 1-bromonapthalene (1-BrNp). With cyclohexanol as our choice for ROH and Gβ-CD as the cyclodextrin, the ternary complex,1-BrNp $\cdot$ Gβ-CD $\cdot$ ROH, forms the basis of the experiments conducted in this thesis. The resultant green phosphorescence exhibited by this supramolecule has a typical lifetime of $\tau \sim 5$ ms. This time-span allows studying a wide variety of flows as discussed further below. Figure 2.1 presents the chemical design and photoluminescence properties of this ternary complex. Without the addition of ROH, only fluorescence is observed (as indicated as curve A), while with the ROH present in the triplex, a bright phosphorescence is achieved (curve B). This light emission forms the basis of measuring velocity using MTV.

Upon excitation by photons of an appropriate wavelength, these molecules are turned into long lifetime tracers. In typical measurements, a pulsed laser is used to 'tag' or 'write' the regions of interest where the velocity vector is sought. This process of tagging can either be done in a one-dimensional form using beam blockers for instance (as shown in figure 2.2 a) or as an intersecting grid of lines, illustrated in figure 2.2 b. Subsequently, these regions are 'interrogated' or 'written' at two successive times within the lifetime of the tracer using an imaging system, e.g. a CCD camera. Thus, the measured Lagrangian displacement between the two 'snapshots' provides an estimate of the velocity component or components.

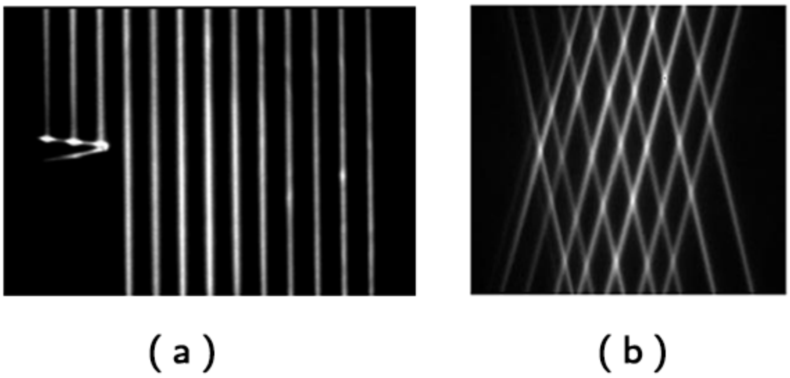

Figure 2.2: Tagging patterns typically used in MTV studies. (a) Multi-line tagging in the trailing region of an airfoil (b) A 7 x 7 tagged grid in a supersonic flow. Adopted from Koochesfahani and Nocera [3]

.

During the past two decades or so, MTV has been adopted to investigate a variety of flows. Some, but not all of these studies, that reflect the diversity of flow conditions in which the technique has found application are:

- In one of the earliest studies involving the aforementioned triplex, Gendrich et al. [2] employed the two-dimensional MTV to study the Lagrangian evolution of reacting and non-reacting mixing interfaces. This was achieved by using a spatial correlation technique to determine velocity as first described by Gendrich and Koochesfahani [38].
- Gendrich and Koochesfahani [39] conducted boundary-layer resolved measurements of leading-edge separation on an airfoil to provide a detailed map of events that occur within the boundary layer at the onset of separation.
- To advance the applicability of the technique, Stier and Koochesfahani [40] performed MTV experiments using biacetyl as a tracer in gas-phase flows. They simultaneously obtained two components of velocity vector (using the grid intersection technique) in a "steady flow" model of an IC engine.

- Thurlow and Klewicki [41] employed the multi-line version of MTV to investigate various regions of turbulence production in a planar Poiseuille-Couette flow. Gas was used as a working fluid. This is one of the earliest studies that advocates the usage of multi-line tagging where the spatial resolution requirements of the experimentation are high. Another example is the work conducted by Hill and Klewicki [42].

- Microscale channel flow in the laminar and transitional regime was studied by Elsnab et al. [43] to understand the validity of macroscale theories. They also concluded that, in their micro channel, the turbulent inertia is the driving mechanism of transitional channel flows.

- Olson et al. [44] employed multi-line MTV to underline the importance of facility-dependent issues during the measurements of the separation and reattachment locations for the steady flow over an airfoil.

- Micro-MTV in gas-phase flows was demonstrated by Samouda et al. [45] and Si Hadj Mohand et al. [46] to investigate Poiseuille flow in a rectangular duct. They demonstrated that the displacement of tagged molecules due to the hydrodynamic motion of was also affected by molecular diffusion, and that this could lead to erroneous measurement of the velocity profiles, if not corrected during post-processing.

- Elsnab et al. [47] performed high-resolution experiments using multi-line MTV in a turbulent channel flow to obtain mean velocity profiles that were twice differentiable. These results were shown to compare well with that of DNS data at similar Reynolds numbers. More recently, they used a similar setup to quantify polymer drag reduction in turbulent channel flow [48] using MTV and assessed the mean-momentum balance framework of [49] with their data.

2.1.1.1 Single-component MTV

For the measurements acquired in the present work, the single-component version of MTV (thereby referred to as 1c-MTV) has been adopted. The fluid domain is tagged along multiple parallel lines which are typically produced using pinhole arrays or beam blockers. Therefore, only the velocity component orthogonal to the tagged line and in the plane of view can be estimated. For such an arrangement measuring the dominant component of velocity, say u, and $\frac{\partial u}{\partial y}$, Hill and Klewicki [42] showed that the relative error associated with these measurements is given as:

$$\frac{\delta u}{u} = \Delta t \, \frac{v}{u} \, \frac{\partial u}{\partial y} \tag{2.1}$$

This is an error estimate in the measured component of velocity primarily due to the influence of other velocity component, v. Therefore, for unidirectional flows with relatively small wall-normal and wall-parallel components of velocity vector i.e. small values of v/u and w/u, the controllable time-delay, Δt, can be adjusted to reduce the measurement errors.

One of the biggest advantages of using 1c-MTV is the spatial resolution the technique offers. Since the tracer molecules are mixed at a molecular level, the spatial resolution of the technique essentially becomes equivalent to the spatial resolution of the imaging system. Therefore, every pixel location corresponds to an independent measurement. In this work, we have taken advantage of this characteristic to fully resolve the relevent length scales in the flow (as discussed briefly in section 1.4).

2.1.2 Molecular Tagging Thermometry

The phosphorescence intensity and emission lifetime of the ternary complex, 1-BrNp · Gβ-CD · ROH, is affected by temperature. This was first observed by Thomson and Maynes [50] in the form of reduced phosphorescence intensity with increasing temperatures. However, a complete framework of measuring temperature through the molecular tagging techniques, referred to as molecular tagging thermometry (MTT), was not established until a series of papers by Hu and coworkers [4, 51, 52].

According to quantum theory [35], the intensity decay of a first-order photoluminescence process from an excited state to its corresponding ground state is described by

$$S_2 = S_1 \, e^{-\frac{t}{\tau}}, \tag{2.2}$$

where τ, the emission lifetime, refers to the time it takes for the initial intensity, S_1, to drop to 37% (i.e. $\frac{1}{e}$) of its initial value. Here, S_2 refers to the intensity at a subsequent time t. The photoluminescence lifetime, τ, is determined by the sum of the rates at which the radiative and non-radiative deactivation processes occur, i.e. $\tau^{-1} = k_r + k_{nr}$, where k_r and k_{nr} are radiative and non-radiative rate constants respectively. According to Ferraudi [53], the non-radiative rate constant is generally temperature dependent, and the resulting dependence of phosphorescence lifetime on temperature forms the basis of measuring temperature using MTT.

Consider imaging a phosphorescence signal at two successive times as required for the velocimetry purpose. The first image is acquired t_0 sec. after the excitation laser pulse for a gate period (exposure) of t_{ex} to produce the phosphorescence intensity, S_1, while the other image is acquired at time $t = t_0 + \Delta t$ for the same exposure to obtain the phosphorescence intensity, S_2, as shown in figure 2.3. Using (2.2), it can be easily shown that the ratio of these phosphorescence signals is given by

$$\frac{S_2}{S_1} = e^{-\frac{\Delta t}{\tau}}. \tag{2.3}$$

(2.3) indicates that the intensity ratio of two successive phosphorescence signals is a

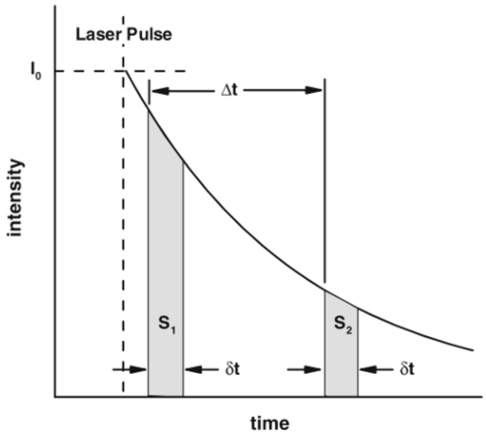

Figure 2.3: A representative schematic of the timing chart for MTT image acquisition. Here, the exposure is represented as δt while the total delay is Δt. Adopted from Hu and Koochesfahani [4]

.

function of the phosphorescence lifetime, τ, and the time delay, Δt, between the two signals. This ratiometric approach, first introduced by Hu and Koochesfahani [51], and further advanced by Hu et al. [52], Hu and Koochesfahani [54], eliminates the issues caused by the spatial and temporal variations in initial incident laser intensity and the artifacts that might occur because of non-uniform dye concentration (e.g. owing to photo-bleaching). It should be noted that if the exposure times of the two images are different, then (2.3) may not be applicable. Algebraic manipulation, the phosphorescence lifetime, τ, therefore can be calculated from (2.3) as

$$\tau = \frac{\Delta t}{\ln \frac{S_1}{S_2}}. \tag{2.4}$$

Therefore, if the temperature dependence of phosphorescence lifetime, τ, is known apriori, then the evaluation of phosphorescence lifetime in a flow-field using (2.4) can be used to generate the corresponding temperature distribution. This apriori *calibration* is described in detail in section 3.1.

2.2 Full depth lock-exchange flow

The primary focus of the present 1c-MTV/MTT experiments is towards understanding the flow dynamics of full-depth lock-exchange flow. Specifically, we are interested to study the configuration in which the initial volumes of the two fluids are identical. The schematic of such a full depth lock-exchange experiment is shown in figure 2.4.

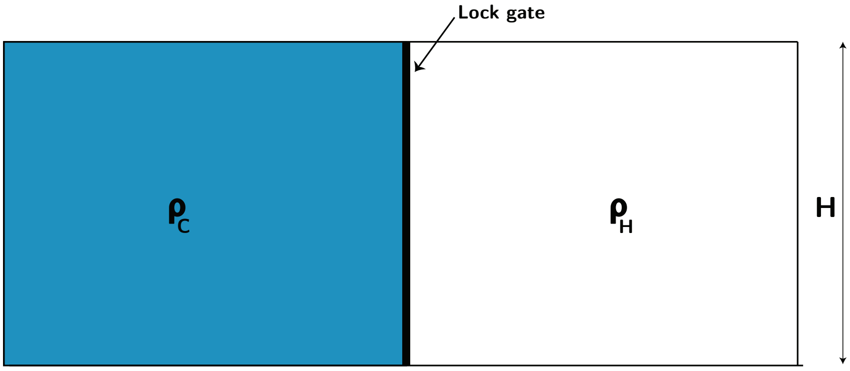

FIGURE 2.4: Schematic of the full depth lock-release experiment. Blue region corresponds to heavy fluid.

We first look at the various evolutionary phases of the resultant gravity current in a general full-depth configuration. Subsequently, we discuss some of the key studies that have addressed the phenomenon of mixing in such currents.

2.2.1 Phases of evolution in a gravity current

Once released from an initial configuration, the present gravity current goes through one or many of the phases now discussed. In each phase, there is a characteristic variation of the front propagation speed that results from the underlying force balance.

Slumping phase

This phase refers to when the heavy fluid "slumps" and forms a sharp gravity current. In this phase, the front of the current maintains a constant speed and thus the current is energy conserving. With the slumping of heavier fluid, the lighter fluid rushes behind to fill the void, and in this process gets reflected from the end wall creating a wave that is called as 'bore'. The slumping phase lasts until the bore catches up with the front, owing to the fact that the propagation speed of the bore is larger than that of the front. This *slumping point*, where the bore overtakes the front, usually lies around 5 - 10 lock lengths from the gate [5]. For the configuration shown in figure 2.4, we do not observe a slumping point due to limited current development length.

Inertial phase

Post slumping point, the gravity current enters a regime where the buoyancy and inertial forces are in balance. During the inertial phase, the current undergoes significant dilution and is no longer energy conserving [14]. Although the front speed decays in a self-similar manner, the body of the current adapts a quasi-steady behaviour [55]. In this regime, the front propagation decreases like $t^{-1/3}$ as first observed by Rottman and Simpson [5].

Viscous phase

Following the inertial phase, the current enters a purely viscous phase where buoyancy and viscous forces are in balance. The current slows significantly during the viscous phase, quantified as $t^{-4/5}$ by Rottman and Simpson [5]. If the viscous forces play a role during the slumping phase, the current skips the inertial phase and directly enters the viscous phase [56]. The front position with respect to initial lock-position as a function of time, as studied by Rottman and Simpson [5] is shown in figure 2.5. However, due to the limited development length in the present experiments, see figure 2.4, we do not observe the inertial and viscous phases.

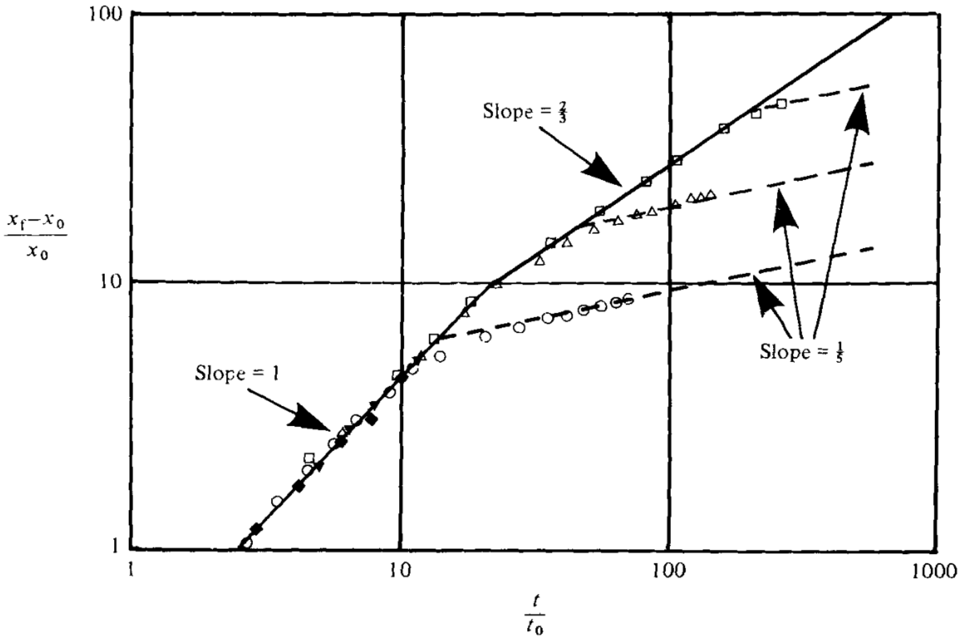

Figure 2.5: Phase transitions in full-depth lock-exchange flows. Markers correspond to different lock-lengths. Slumping phase corresponds to slope being unity while the inertial and viscous phases are marked as regions with slope of 2/3 and 1/5 respectively. Adopted from Rottman and Simpson [5].

2.2.2 Mixing in lock-exchange flows

This section discusses the key findings of previous studies that have investigated lock-exchange mixing. The presentation is not restricted to studies that used the present experiment configuration and considers both experimental and numerical findings.

One of the earliest lock-exchange studies was conducted by Hacker et al. [31]. Their experiments used a back-lighting system and established a correlation between the absorbed light by the dye and the fluid density. The density structure of the current was then inferred from the dye concentration. They observed the breaking of Kelvin-Helmholtz waves that produced stratified fluid in the rear of the current. From an examination of isopycnals, they concluded that the fluid inside the gravity current progressively dilutes with the front propagation. Quantifications pertaining to mixing were not, however, provided in this work.

To quantify the mixing during slumping phase, Fragoso et al. [33] used the background potential energy approach introduced by Winters et al. [22] and described in detail in section 1.2.1.3. They used an experimentation technique similar to that of Hacker et al. [31]. Fragoso et al. [33] found that the density threshold chosen to understand dilution of the current significantly affected the measured mixing in the vicinity of slumping point. This problem, however, diminishes with an increase in measurement resolution. For a two-dimensional measurement plane, they estimated the total and background potential energy and showed that the background potential energy of the system increases monotonically.

The direct numerical simulations (DNS) of Ilıcak [57] provide an estimate of the mixing efficiency as given by (1.28). From this study, they concluded that the Kolmogorov length scale (λ_K) must be resolved, but not necessarily the Batchelor scale (λ_B), (see (1.29)), if the convergence of background potential energy is sought. Based on the front speed and height of their computational domain, they perfomed simulations for a Reynolds number (Re) range of 125 to 10,000. Ilıcak [57] reported that the mixing efficiency in a lock-exchange experiment saturate at approx. 0.12 for $Re > 2500$.

Hughes and Linden [58] used a full-depth lock-exchange configuration similar to the one studied in this thesis. They measured the density fields before and after the experiment and based on the fraction of initial potential energy spent towards mixing, they calculated an asymptotic mixing efficiency of 0.08. They quantified mixing efficiency as $\frac{PE_f - PE_{nm}}{PE_i - PE_{nm}}$, where PE_i and PE_f correspond to the potential energies at the start and end of the experiment while PE_{nm} denotes the potential energy of a final state where no mixing takes place between the two fluids. They further showed that the mixing associated with such flows attains a self-similar state only at Reynolds numbers greater than about 50,000.

Through simultaneous measurements of velocity and density field using a two-dimensional PIV-PLIF setup, Balasubramanian and Zhong [21] measured entrainment coefficients, E_F, for a partial-lock configuration. They calculated E_F at the front and the head of the propagating current and observed that higher values were obtained near the front due to vortex generated mixing. It was shown that Holmboe wave type instabilities were associated with lower Reynolds numbers while Kelvin-Helmholtz breakups corresponded to high Reynolds number flows and involved greater mixing.

To the best of the present author's knowledge, there has not been any experimental study to directly evaluate mixing efficiency using (1.27) or (1.28). In this regard, Ilicak [59] notes that λ_K must at least be resolved to yield satisfactory and convergent results. This is where the present work seeks to fill the gap in our current understanding of full-depth lock exchange flows. With 1c-MTV/MTT, we are able to obtain spatially resolved estimates of simultaneous streamwise velocity/temperature(density) fields. These estimates allows one to calculate the instantaneous mixing efficiency, (1.27), and overall mixing efficiency, (1.28). The details regarding how this is accomplished is given in subsequent chapters.

Chapter 3

Experimental Description

This chapter presents details pertaining to the experiments conducted. The following narrative is broadly divided in two parts:

- A general implementation of MTT calibration is described. This includes various components that comprise typical 1c-MTV/MTT experiments. This calibration establishes a mathematical relationship between the phosphorescence lifetime and the fluid temperature, and forms the basis of measuring temperature using MTT.
- The second part of this chapter focuses on the lock-exchange experiments. Here, we first present the dye visualizations that were conducted to investigate the mean properties of gravity current. The details of the 1c-MTV/MTT experiments addressing the questions posed in section 1.4 are then presented.

3.1 Implementation of MTT calibration

As described in section 2.1.2, phosphorescence lifetime of the ternary complex, 1-BrNp $\cdot$ Gβ-CD $\cdot$ ROH, is highly temperature dependent. Therefore, to establish an *aprioi* mathematical relationship between the phosphorescence lifetime, τ, and the temperature, T, we employ a calibration procedure similar to that of Hu and Koochesfahani [54]. The schematic of this system is shown in figure 3.1. Since the individual components shown in figure 3.1 remain identical for a 1c-MTV/MTT experiment, these are now discussed before the calibration results are presented.

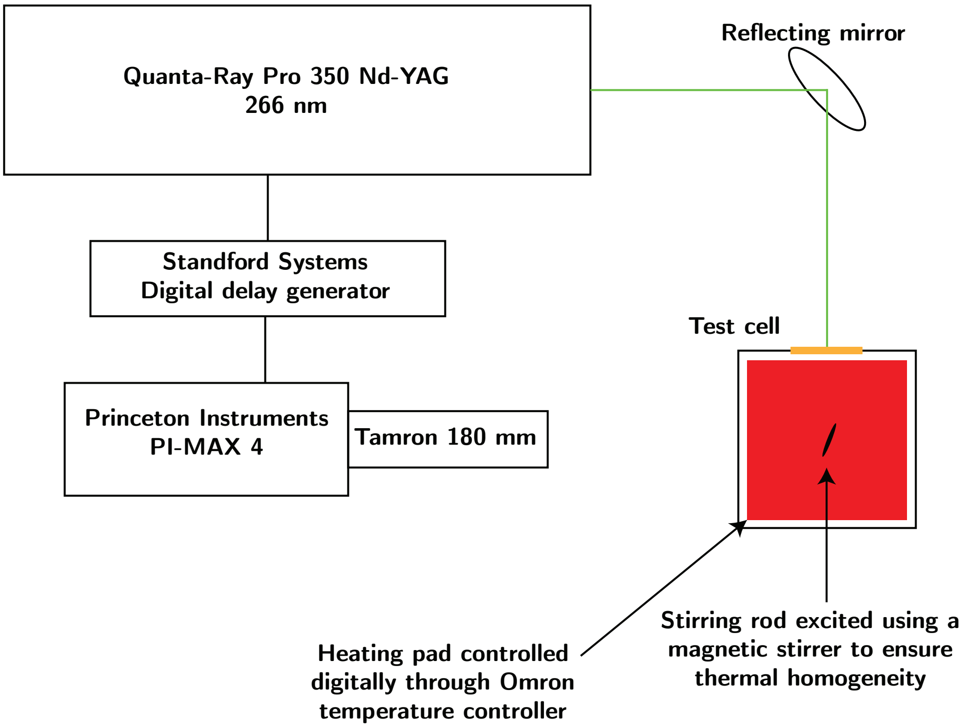

FIGURE 3.1: Schematic of the set-up used for temperature calibration

Flow tagging

The tracer molecules are tagged using a fourth harmonic Quanta Ray Pro-350 Nd:YAG laser (wavelength, λ = 266 nm) manufactured by Spectra Physics. The beam energy peaks at 250 mJ/pulse and the present experiments are conducted at approximately 25 - 30 % of the maximum beam energy. This is done in order to avoid photobleaching in a dual-temperature fluidic system. The beam is manipulated and guided using a series of mirrors before transmitting through the fused-silica window located on one side of the test cell (see figure 3.1) that contains an aqueous solution of 1-BrNp $\cdot$ Gβ-CD $\cdot$ ROH. The volume of this cell is approxi 1.5 L. The original work of Hu and Koochesfahani [54] employed a 308 nm UV laser which exhibits less attenuation as compared to the laser wavelength used for the present measurements. To compensate for this, we halved the concentration of cyclodextrin, Gβ-CD, that was used for making the triplex as per the recommendation by Gendrich et al. [2]. Individual laser lines were formed by passing the beam through a pinhole array. The diameter of these pinholes (d) vary from 0.5 - 1 mm whereas the corresponding pitch (p) varied between 2 - 4 mm. Unless otherwise stated, the measurements correspond to $d = 0.75mm$ and $p = 4mm$.

Bulk temperature monitoring and control

The temperature of the test cell was measured using a pair of Omega HH41 thermistors (measurement accuracy = $\pm 0.015^o C$), while the control was achieved using a digital temperature controller, Omron E5CC. A surface heating pad was attached to the base of the test cell. It was triggered using the output of a solid-state relay connected to the temperature controller. Polystyrene sheets were attached to the side walls to thermally insulate the test cell. The apparatus was stirred magnetically in order to achieve thermal homogeneity within the test cell. Additionally, another K-type thermocouple (measurement accuracy = $\pm 1^o C$) along with the thermistors monitored the thermal equilibrium during the calibration process. For these measurements, we observed a measured temperature uniformity of $\leq 0.1^o C$ within the test cell.

Flow interrogation

The resulting phosphorescence was imaged through a dual-frame gated intensified CCD (ICCD) camera, Princeton Instruments PI:MAX4. This camera provides an image size of 1024 x 1024 pixels. The reasons why an ICCD camera was deployed are multi-fold. Firstly, the intensifier produces the required signal to noise ratio needed to accurately determine the MTV line positions. The importance of a high S/N is highlighted in the study of Ke and Bohl [60]. Second, this camera allows one to acquire image pairs on the same imaging array for each instantaneous set of measurements. One limiting attribute of the ICCD camera is the presence of a fixed background spatial pattern, referred to as the *chicken wire* pattern. This pattern is associated with the fiberoptic coupling internal to the camera. The chicken wire pattern introduces a low level spatial noise into the acquired images that creates difficulty in obtaining derivatives with high accuracy [47]. A flatfield normalization as outlined by Bohl [61] is used to remove the errors largely attributed with this chicken wire pattern. This is described in section 3.2.3.

MTV Timing diagram

A digital delay generator, Stanford DG645, was used to synchronize the laser with the ICCD camera. The software interface, Lightfield, provided by the camera manufacturer controlled the timings of the initial and the final laser pulse to within 1 ns. Corresponding exposure times (gate width) were also controlled using Lightfield. A general timing diagram for the measurements is shown in figure 3.2.

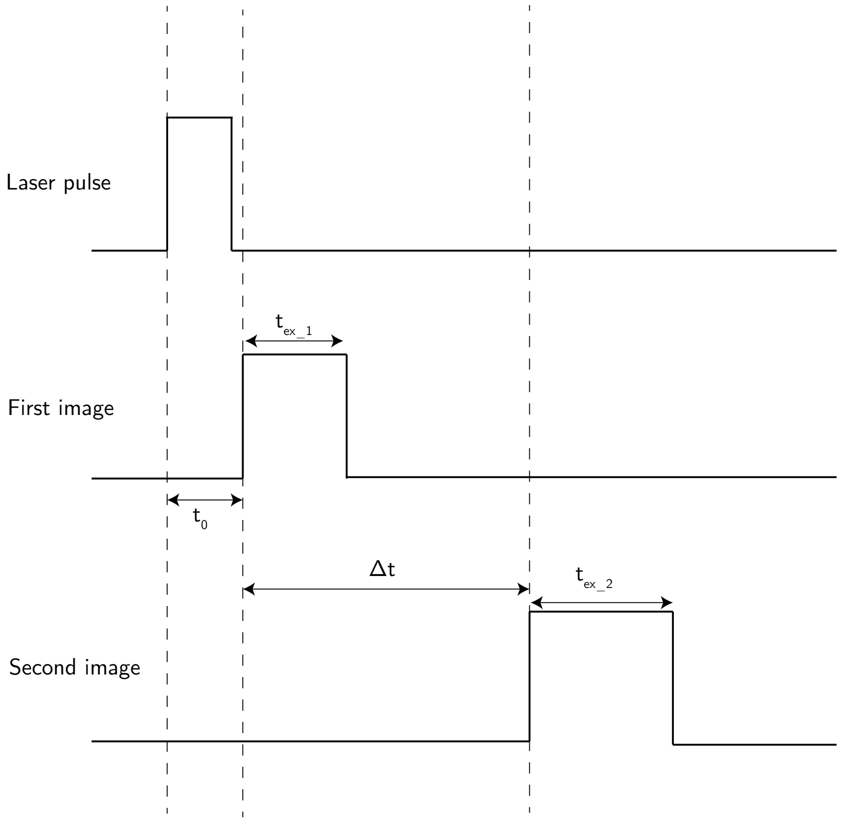

FIGURE 3.2: A representative timing diagram illustrating the various time delays associated with the measurement process. Both the images are acquired using the same camera in successive frames. For the present measurements, $t_{ex_1} = t_{ex_2}$.

3.1.1 MTT calibration curve

The calibration begins with the heating of an aqueous solution of 1-BrNp · Gβ-CD · ROH to a pre-determined temperature, T. Once the solution attains thermal equilibrium, phosphorescence signals at two successive times, $t_o = 5\mu s$ and $t_o + \Delta t = 4.5ms$, were acquired. These timings were selected after a careful inspection of the requirements of time delays in a lock-exchange experiment (discussed further in next chapter). These signals provide an estimate of phosphorescence lifetime, τ, through (2.4). This process was repeated for a range of solution temperatures from 15 to 40° C.

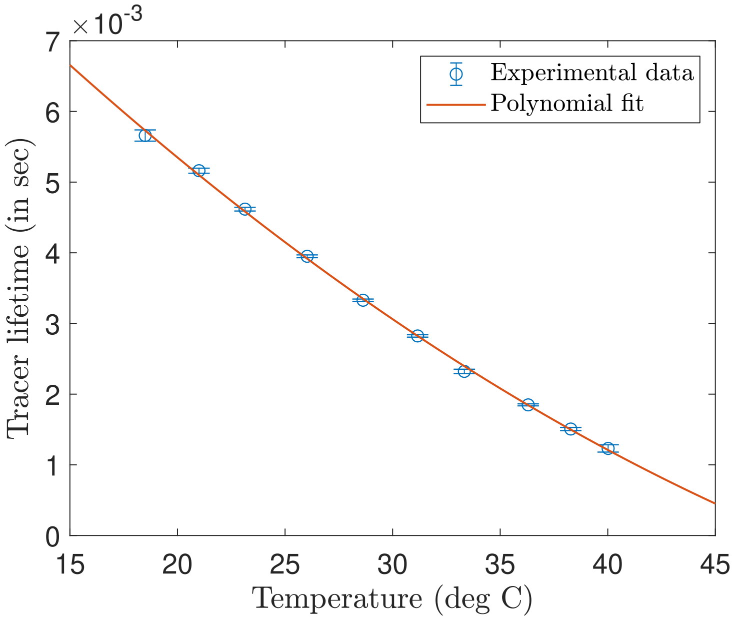

Figure 3.3: Variation of tracer lifetime as a function of temperature. Vertical bars represent the extent of variation in lifetime for 250 image pairs.

An example of the tracer lifetime as a function of fluid temperature, $\tau(T)$, is shown in figure 3.3. While the lowest temperature in figure 3.3 is restricted by the ambient conditions, a poor S/N ratio at the other extreme poses a limit to the maximum permissible temperature. A second-degree polynomial is sufficient to fit the experimental data, as shown in the figure.

Hu and Koochesfahani [54] noted that this calibration, $\tau(T)$, suffers from an 'aging' effect. Therefore, one must use a normalized version where the phosphorescence lifetime is normalized by its value at a reference temperature. Using a reference temperature of 25 ^{o}C, the variation of normalized lifetime is shown in figure 3.4. We use the fitted polynomial to infer the temperature distribution in a fluid flow when the corresponding phosphorescence lifetime distribution is known.

Spatial attenuation effect

As mentioned previously, the light beams (λ = 266 nm) used for the present experiments exhibit a noticeable attenuation as they traverse the solution. Therefore, in order to critically analyze the spatial homogeneity of phosphorescence lifetime at a given temperature level, a plot of tracer lifetime as a function of penetration depth, $\tau(y)$. is shown in figure 3.5.

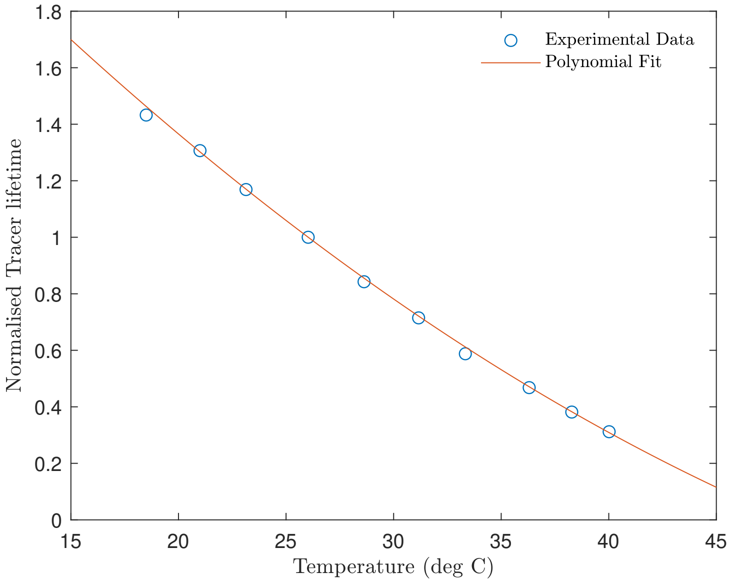

FIGURE 3.4: Variation of normalized tracer lifetime as a function of temperature. Reference temperature = 25 ^oC.

The y-axis on the left (blue) shows the variation in the instantaneous phosphorescence intensities obtained at times t_o (solid) and $t_o + \Delta t$ (dashed). It can be observed that the emitted phosphorescence attenuates significantly owing to a combination of non-parallel beam propagation and due to the presence of salts, i.e. cyclodextrin. However, the corresponding instantaneous lifetime, shown on the y-axis on the right (red), remains almost constant, as indicated by the dashed line that represents the mean lifetime at the same temperature. The uncertainty in temperature measurement corresponding to the standard deviation of the instantaneous phosphorescence lifetime is 0.15^o C.

3.2 Lock-exchange experiments

A detailed description of the lock-exchange experiments is now presented. Prior to the 1c-MTV/MTT experiments, multiple dye visualizations were conducted in order to measure and validate the mean properties of the gravity currents e.g. Froude number, Fr. Based on the estimates derived from these visualizations, the parameter space for the 1c-MTV/MTT experiments was determined as discussed later.

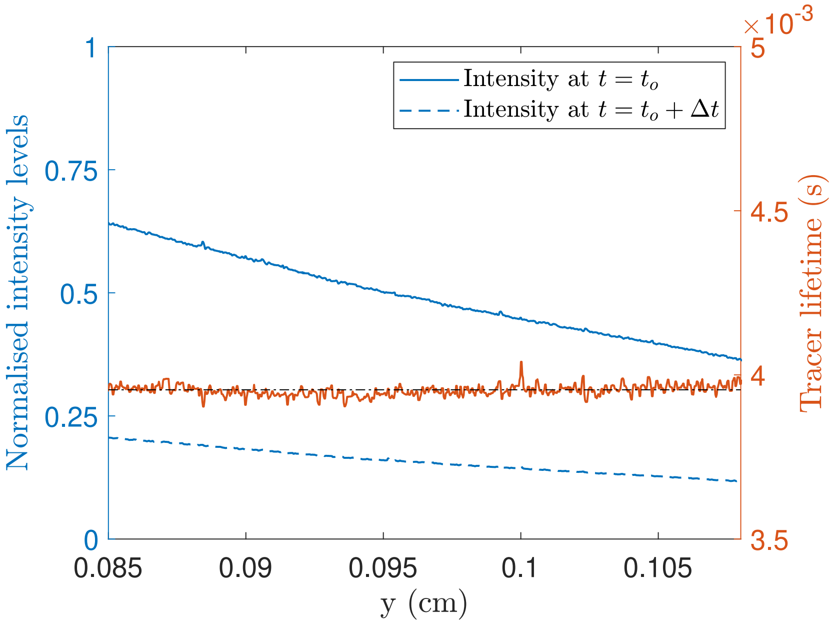

FIGURE 3.5: Spatial variation of tracer lifetime along the wall-normal direction, y. Black dash-dotted line represents the mean lifetime value.

3.2.1 Facility

The present measurements were acquired in a Perspex tank of length 2 m which has a uniform cross-section of 0.2 m × 0.2 m; see figure 3.6. The lock-gate (a thin metallic plate) in this facility was placed at the centre to minimize transitions in the flow related to end-wall reflection. Before the experiment commences, fluid was filled on either side of the gate. For the case of dye visualization, water was used as the fluid. While, for 1c-MTV/MTT measurements, it was an aqueous solution of 1-BrNp · Gβ-CD · ROH. Subsequently, the fluid on one side of the lock was heated in order to achieve the desired reduced gravity, g', where $g' = g\left(\frac{\rho_C - \rho_H}{\rho_H}\right)$; ρ_C and ρ_H being the fluid densities corresponding to cold and hot fluid respectively. During heating, the fluid was continuously stirred using a pair of submersible pumps to ensure thermal homogeneity. Bulk fluid temperatures were monitored using multiple Omega HH41 thermistors (measurememnt accuracy = $\pm 0.015^o C$). The experiment commences with a rapid removal of lock-gate. A lever-switch, connected to the lock-gate, triggers the initiation of the data acquisition process.

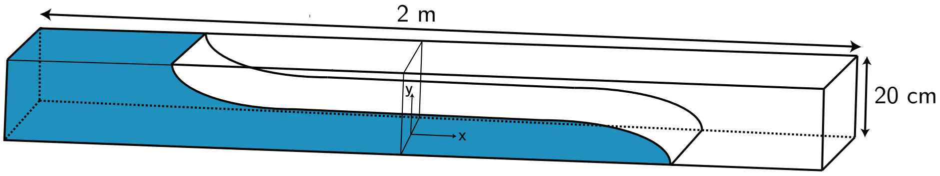

FIGURE 3.6: Schematic of the experimental facility. Shaded region corresponds to cold (heavy) fluid.

3.2.2 Dye visualization

Two types of dye-based experiments were conducted with an overarching aim to study the mean properties of the gravity current. First, the current development area, i.e. from the lock's location to end wall, was studied using a laundry brightener as dye. These experiments are referred to as dye visualization 1 or *DV1*. The mean velocity and height of the gravity current was measured through these visualizations. Finally, fluorescein-dye based visualizations, referred to as *DV2*, were carried out to qualitatively examine the occurrences of Kelvin-Helmhotlz like instabilities at the interface of the gravity current that would also feed into our attempt to understand instantaneous mixing efficiency.

DV1 Experiments

Once the desired temperature difference was established across the lock, a small amount of laundry brightener, Blue-O, was added to the cold fluid. This allows one to distinguish the current from the ambient fluid (see figure 3.7). The resulting gravity current was recorded using three Nikon D810 DSLR cameras paired with a Nikon Nikkor 60mm F/2.8 lens at a frequency of 60 Hz. Images from the individual cameras were stitched together in MATLAB to produce the field of view (FOV) required for analysis. An example of a stitched image is shown in figure 3.7. These visualizations allowed a tracking of the front location, thereby estimating the velocity. Noting the front depth, one can obtain the Froude number, $Fr = \frac{U}{\sqrt{gH}}$. These results are discussed in the next chapter. The parameter space for these visualizations is presented in table 3.1. The slight run-to-run variation in temperature across these experiments ($1\ ^oC$) is attributed to the ambient temperature at which the cold fluid was maintained. An additional set of experiments, parametrically similar to table 3.1, were conducted using table salt to induce the initial density difference. The purpose of these experiments was to verify that our experiments

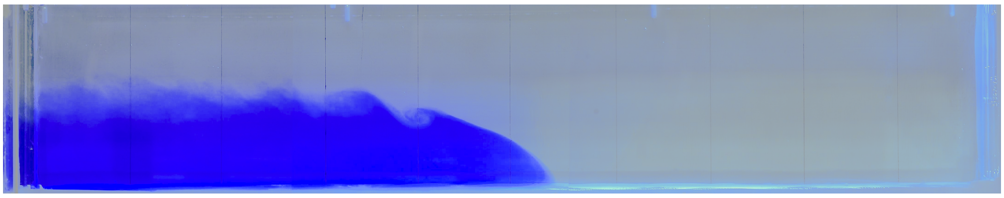

FIGURE 3.7: Gravity current as studied using a typical DV1 experiment using Blue-O dye. The current is traveling from left to right. $g\prime \sim 40\ mm/s^2, t = 11sec$.

$T_C(^oC)$	$T_H(^oC)$	$g'(mm/s^2)$	Experimental runs
20 ± 1	35 ± 1	~ 40	2
20 ± 1	40 ± 1	~ 55	2

TABLE 3.1: Experimental parameters for the DV1 experiments.

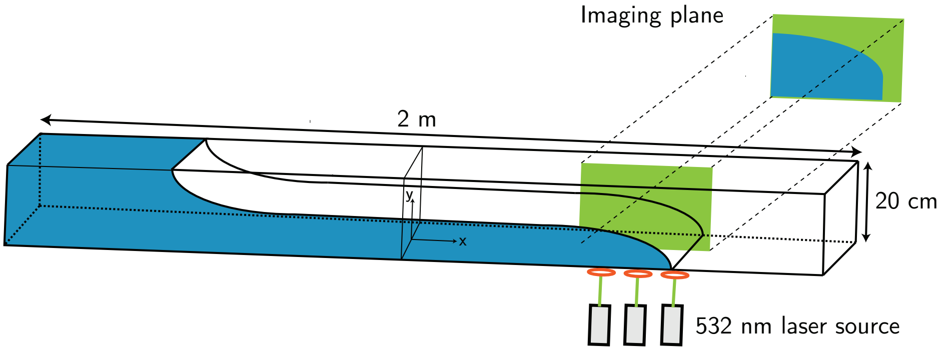

FIGURE 3.8: Schematic of the DV2 experiments. Three lasers are used to create a 25 cm wide laser sheet.

compare-well with those of the previous lock-exchange studies that employed a salinity based stratification [13, 32, 56, 62–64].

DV2 Experiments

Since the primary focus of the *DV1* visualizations was on the bulk flow properties, a refined set of experiments were conducted to examine the effect of the interfacial instabilities. These instabilities, e.g. 2D or 3D Kelvin-Helmholtz waves, Holmboe instability etc., are a key feature of counter-travelling gravity currents [5, 10, 21, 30, 58]. To examine these phenomena, a laser sheet (width $\sim$ 25 cm and thickness $\sim$ 1 mm) was created in the centre of the development regime using three 532 nm lasers and suitable optics. The horizontal span of the laser sheet ranged from a distance of $x = 25$ cm to $x = 50$ cm from the lock as shown in figure 3.8. A small amount of fluorescein dye (mass = 0.1 gm,

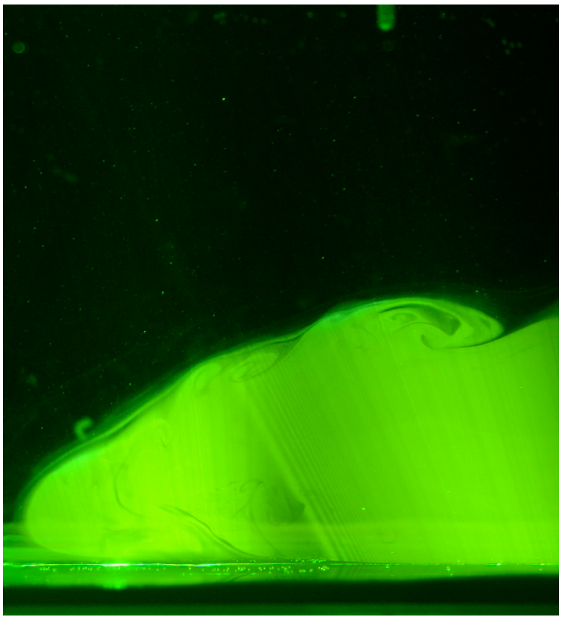

FIGURE 3.9: An example image from a typical DV2 experiment. The current is travelling from right to left. $g\prime \sim 40\ mm/s^2, t = 11 sec$.

provider - Sigma Aldrich) was mixed with the cold fluid to visualize the flow. A Nikon D800E DSLR camera was mounted with a 50mm F/1.8 to record the gravity current at 60 fps. A snapshot from a *DV2* visualization is shown in figure 3.9. The parameter space of these experiments is identical to that of *DV1* (table 3.1). Detailed analysis of these visualizations and the corresponding results are presented in section 4.1.

3.2.3 1c-MTV/MTT Experiments

Mean behaviours of the gravity current produced in the facility were validated through dye visualizations. These results establish the parameter space for the 1c-MTV/MTT experiments that are now described. The facility was filled with an aqueous solution of 1-BrNp · Gβ-CD · ROH at the start of the experiment. Heating and thermal control was carried out in a manner similar to that of dye visualization. Individual MTV lines were created using a finer pinhole array (d = 0.75 mm, p = 2 mm) from the same source employed for MTT calibration (λ = 266 nm). The reasoning behind using a finer pitch pinhole array is to get a larger number of MTV lines in the measurement FOV. This allows an approximate calculation of spatial derivatives in the streamwise direction. However, as discussed later, for better estimates of streamwise derivatives, a greater number of pinholes are needed.

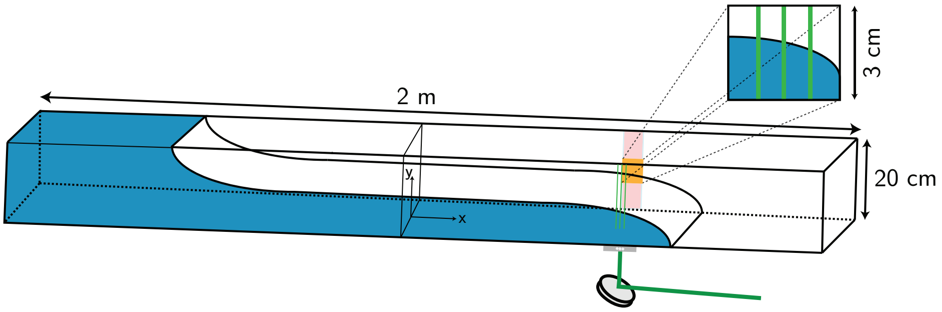

FIGURE 3.10: Schematic of the 1c-MTV/MTT experiments. Three laser lines are observed in the FOV.

The resulting phosphorescence signal was imaged through an optical glass (shown using pink colour in figure 3.10). For the present experiments, the first image was acquired $t_o = 5\mu s$ after laser emission. This slight delay is used to remove the emitted fluorescence from the chemical tracer that decays to immeasurable intensities within 1-2 μs. The time delay between successive images was set to 4.5 ms - 5.5 ms depending upon the initial g'. These parameters were established after carefully considering the mean front velocity and the imagable phosphorescence lifetime of the molecular triplex in the range of temperatures involved. The images were obtained by exposing the sensor for a period of 1 ms. The relatively long delays and exposure times are associated with the low flow velocities. During these experiments, the image pairs are acquired at a rate of 5 Hz.

The FOV of the measurements begins at a height of $y \approx 8.3$ cm from the bottom wall and ends at $y \approx 11.3$ cm (see the orange square in figure 3.10). The size of this FOV is restricted by the resolvable displacements for the velocity measurements, whereas it is less dependent on the temperature being measured. With an output image size of 1024 × 1024 pixels, the measurement technique effectively probes the interfacial region with a spatial resolution of $\Delta y \approx 0.025$ mm. Figure 3.11 shows the lock-exchange flow facility with the associated experimental components.

As shown later, these measurements were able to resolve the smallest velocity dissipation scale (λ_K) and get close to resolving the scalar dissipation scale (λ_B). Based on the results of visualizations and the limiting technicalities associated with 1c-MTV/MTT measurements, the feasible parameter space for the present experiments are summarised in table 3.2.

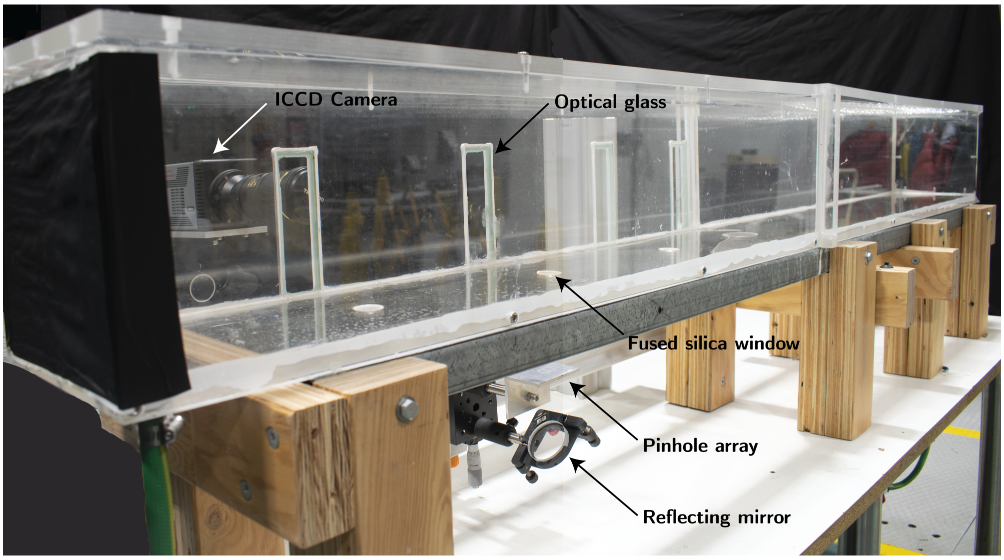

Figure 3.11: Lock-exchange flow facility presenting the various components.

$T_C(^oC)$	$T_H(^oC)$	$g'(mm/s^2)$	$Re = \frac{UH}{\nu}$	Experimental runs
20 ± 2	30 ± 2	~ 25	$\sim 7{,}000$	20
19 ± 3	34 ± 2	~ 40	$\sim 10{,}000$	20

Table 3.2: Experimental parameters for MTV/MTT experiments. Reynolds number is calculated based on the front speed (estimated through dye visualization) and tank height.

Data post-processing

Following acquisition, the images were spatially smoothed using a five-point median filter at each wall-normal location. The aforementioned spatial chicken-wire pattern was corrected by normalising individual pixel intensities using the corresponding darkfield and flatfield images, hereby referred to as DF and FF respectively [47]. The dark image, DF, was acquired after putting the lens cap on the camera lens while the flatfield image, FF, was obtained by exposing the camera sensor to a uniformly lit background. These images were taken under identical timing conditions, e.g. exposure time, intensifier gain etc., as those used during the experiments. For any instantaneous image, I, the normalized image, I_C, is given by

$$I_C(x_i, y_j) = \frac{I(x_i, y_j) - DF(x_i, y_j)}{FF(x_i, y_j) - DF(x_i, y_j)}. \tag{3.1}$$

A sample instantaneous image pair after the flatfield normalization is shown in figure 3.12. Here, the first image is taken after 5 μs after laser pulse and the interframing delay

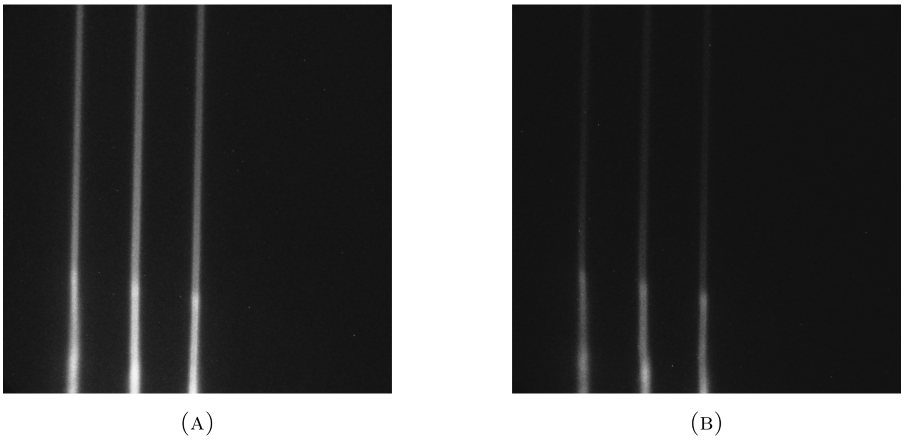
(A) (B)

FIGURE 3.12: Instantaneous image pairs obtained from a $g' \sim 40$ mm/s^2 case. In (B), the brighter bottom half corresponds to colder fluid i.e. slower decay owing to longer lifetime.

between the two images is set to 3.5 ms. Lagrangian displacements were determined from these instantaneous images via use of an FFT-based cross-correlation at each pixel location along the wall-normal direction. This technique is described in greater detail in [38]. To obtain sub-pixel accuracy, a second-order polynomial was fit through the peak in the correlation distribution as suggested by Gendrich and Koochesfahani [38]. The 95% confidence interval for MTV measurements using the present camera is 0.3 pixel. This estimate is based upon the method outlined by Bohl [61]. Prior to lock-exchange experiments, this data reduction algorithm was implemented in a turbulent channel flow. The results were found to agree very well that of the DNS data and are presented in appendix A.

To obtain the temperature field for each wall-normal location, the peak intensity values were located in both images. The average intensity in a small window around this peak (9 pixels in the streamwise and 5 pixels in the wall-normal direction) was used to determine the corresponding signals, S_1 and S_2 respectively for the undeformed and deformed images. (2.4) was used for every pixel (in vertical direction) to calculate the tracer lifetime, τ, based on these phosphorescence signals. These values of τ provide an estimate of the fluid temperature using the calibration established in section 3.1.1.

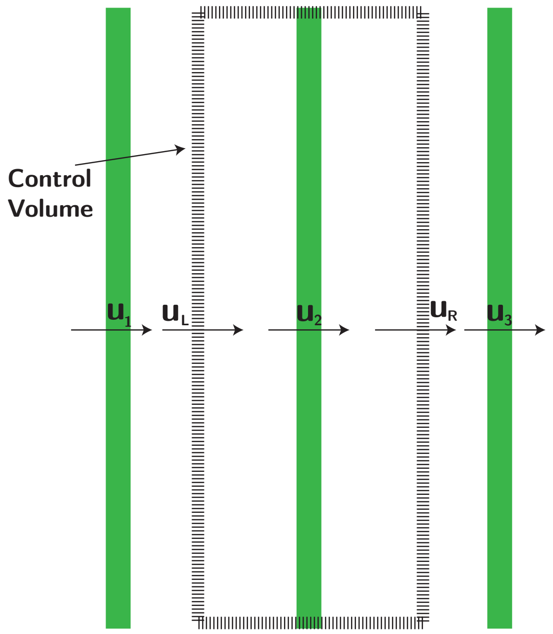

FIGURE 3.13: Sketch of the control volume considered to quantify (1.23) and (1.27). Green lines represent 1c-MTV/MTT measurement lines.

Flow energetics and mixing efficiency

Given the temperature distribution, the corresponding density field was obtained using the relation provided by Hyland and Wexler [65]. To estimate the background potential energy (see 1.20),these estimates of $\rho(y)$ were subsequently 'sorted' in wall-normal direction. A control volume, as shown in figure 3.13 was considered for further analysis. The face parameters of this control volume, e.g. u_L and u_R, were interpolated from the correspondingly obtained multi-line measured values, e.g. u_1, u_2 and u_3. (1.23) was then used to calculate the instantaneous mixing rate, $\mathcal{M}$. The derivatives involved in this estimation were calculated using a cubic-splines based curve fitting method [66]. Finally, the viscous dissipation, ϵ, was quantified by invoking the isotropic flow relations, yielding

$$\epsilon = \frac{15\nu}{2}\left(\frac{\partial u}{\partial y}\right)^2 . \tag{3.2}$$

To avoid any irregularities associated with a time-varying phenomenon, we have further smoothed the data using a 3-points median filter and followed by a 3-points moving mean filter (in time). Finally, mixing efficiencies are estimated using (1.27) and (1.28).

Chapter 4

Results

This chapter presents the main findings of this study. First, the results from various dye visualization experiments are discussed. These are compared with findings in the existing literature to validate the facility and phenomena under study. Next, the velocimetry and thermometry data obtained through the 1c-MTV/MTT measurements are presented. Details associated with the measurement accuracy are then discussed. Results from individual experiments, as well as the collective ensemble data, are presented to address the time variability of the flow. This is followed by a discussion on the interfacial properties where the shear and its time evolution are quantified. Finally, the analysis of lock-exchange mixing is presented. The evolution of background potential energy and the corresponding estimates of mixing efficiencies, (1.27) and (1.28) respectively, concludes this chapter.

4.1 Dye visualisation

Two types of dye visualizations were carried out. In the first type of visualizations, referred to as *DV1*, a colored dye was homogeneously mixed in the cold fluid to reveal flow features and quantify the mean properties of the gravity current, e.g. depth, front velocity etc. In second set of visualization experiments, referred subsequently as *DV2*, a *planar section* in the flow field was visualized using fluorescein dye. The aim of these experiments was to qualitatively analyse the interfacial flow features in a gravity current.

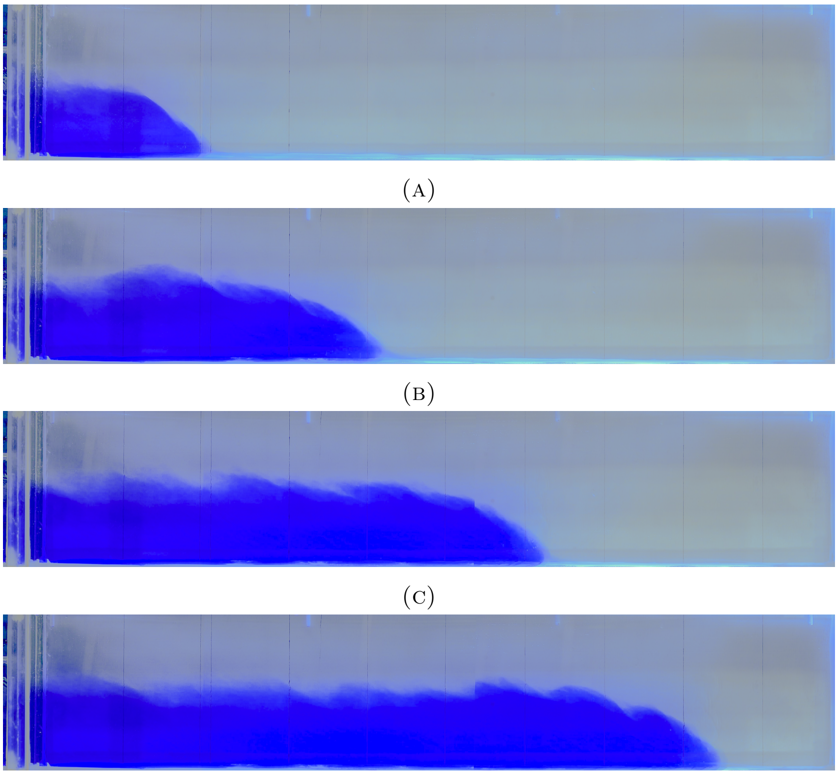

(A)

(B)

(C)

(D)

Figure 4.1: Snapshots from a *DV1* experimental run ($g' \sim 40\ mm/s^2$) after (A) $t = 5$ sec, (B) $t = 10$ sec, (C) $t = 15$ sec and (D) $t = 20$ sec. Lock is present at the extreme left of the FOV while the extreme right corresponds to a side wall.

For the case of $g' \sim 40\ mm/s^2$, the stitched images from the *DV1* experiment depicting the flow evolution are presented in figure 4.1. Upon lock removal, the heavy fluid slumps as a result of difference in hydrostatic pressure as evident from figure 4.1a. Figures 4.1b to 4.1d illustrates further advancement of the gravity current and suggests that the current occupies approximately half the total tank height, which would be quantified later. We stop collecting the experimental data once the current hits the end-wall.

The front velocity was estimated by tracking the sharp nose (right-most point corresponding to the blue region) at various time instants. The current depth was estimated based on the vertical location where the dye intensity concentration changed abruptly. The estimate of the front velocity also allowed us to determine the time delays required for the 1c-MTV/MTT measurements.

Figure 4.2 presents the comparison of non-dimensional front position, $\frac{x_f}{H}$, as a function of non-dimensional time, $t^* = t\sqrt{\frac{g(1-\gamma)}{H}}$, where H is the tank height and $\gamma = \frac{\rho_H}{\rho_C}$. The density ratio, γ, is used to allow a direct comparison of these results with that of Shin et al. [6]. They conducted salt-based lock-exchange experiments ($Sc \sim 700$) in a facility identical to the one used in the present study. Therefore, comparing the two findings provides a quantitative estimate of the differences as a result of thermal stratification with $Sc \sim 7$. The slope of the data corresponds to the front Froude number, $\frac{U}{\sqrt{g'H}}$ (recall equation 1.2). $Fr = 0.5$ indicates that the current is energy-conserving and would occupy exactly half the total tank height. The present measurements yield a $Fr \sim 0.48 \pm 0.02$ which, not surprisingly, is similar to that of Shin et al. [6]. This suggests that there is no substantial impact of the Schmidt number on the mean properties of a gravity current. This behaviour is also observed in the numerical simulations of Bonometti and Balachandar [67] who noted that the macro properties of the flow are not affected by the changes in Schmidt number (they varied Sc from 1 to ∞).

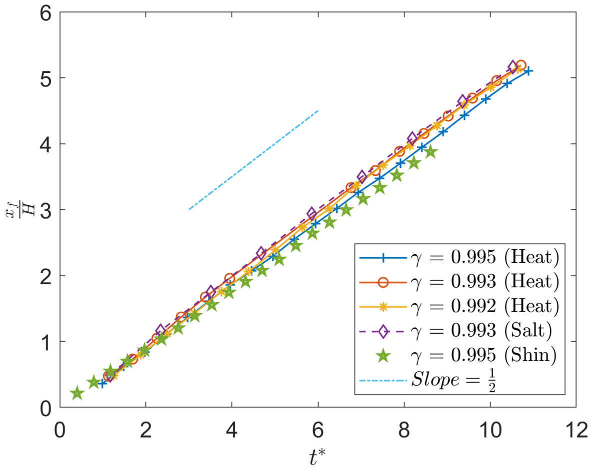

FIGURE 4.2: Head location normalised with total depth, H, as a function of dimensionless time $t^* = t\sqrt{\frac{g(1-\gamma)}{H}}$ where t is time in seconds. (Shin) refers to Shin et al. [6].

Images from a *DV2* experiment for the case of $g' \sim 40\ mm/s^2$ are presented in figure 4.3. Here, the light source (laboratory-grade green laser, $\lambda = 532$ nm, power = 0.5 W) fluoresces the dye mixed with the cold fluid and the field of view spans approximately 20 cms in the direction of current propagation. The direction of the flow is from right to left. The planar nature of these visualizations allowed us to examine the two-dimensional flow features that occur at interface. For instance, a vortical overturn, that develops at $t = 11$ sec and subsequently breaks down at $t = 15$ sec, can be observed from these images. Such features, as well as other instabilities, e.g. two and three-dimensional Kelvin-Helmholtz vortices, Holmboe waves are very commonly observed at the interface of counter-travelling gravity currents [5, 21, 58, 68]. Froude number, Fr, obtained from these experiments had a value identical to that of the *DV1* experiments.

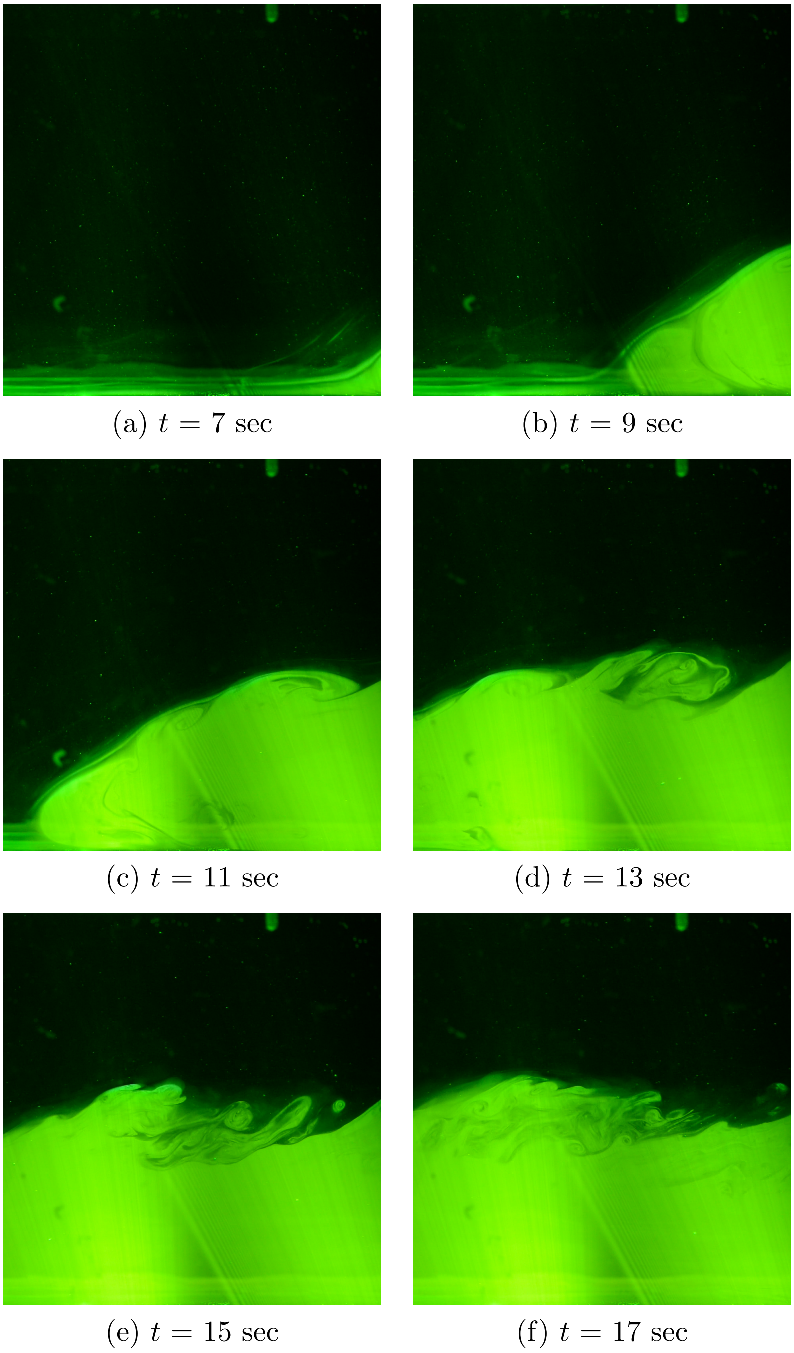

(a) t = 7 sec

(b) t = 9 sec

(c) t = 11 sec

(d) t = 13 sec

(e) t = 15 sec

(f) t = 17 sec

FIGURE 4.3: Snapshots from the fluorescein dye based visualisation ($g' \sim 40\ mm/s^2$) at various times. The gravity current is travelling from right to left.

The flow evolution corresponding to this visualization is presented in the form of a space-time plot in figure 4.4b. To obtain this diagram, intensity data corresponding to a vertical cross-section, as shown by the red line in figure 4.4a, was plotted against time. This procedure allows mimicking the 1c-MTV/MTT based experimentation where

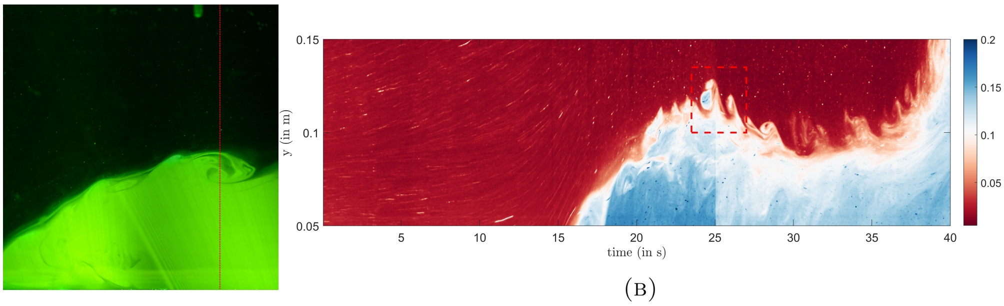

(A)

(B)

FIGURE 4.4: (A) Gravity current for the *DV2* experiment at t = 18.5 sec. Vertical red line corresponds to the probed spatial location for the space-time diagram. (B) Spatio-temporal variation of the dye intensity (arbitrary values). Square marks the signature characteristic of an overturn event as observed during the visualization.

the flow domain is probed using a laser 'line'. As can be observed, the gravity current arrives at this line location at $t \sim 15$ sec (see figure 4.4b) and occupies roughly half the tank height (refer to the y-axis, where $y = 0.1$ m marks the half tank height). These visualizations also provided a way to obtain the 'signature' of such interfacial features, e.g. vortical overturns in the corresponding space-time contours. This signature is identified by the red square in figure 4.4b. As discussed later, these signatures are very useful in identifying the occurrence of such important flow features or similar events during a 1c-MTV/MTT experiment, where we have no access to images like figure 4.4a.

4.2 Velocimetry and thermometry results

The results obtained through the 1c-MTV/MTT experiments are now discussed. As mentioned in section 3.2.3, 20 independent experiments were conducted for each of the two cases of $g' \sim 25$ mm$/s^2$ and $g' \sim 40$ mm$/s^2$. For the sake of demonstration, however, data from random trials corresponding to each of the two cases is presented. The scatter across these experiments and the associated run-to-run variability are discussed later.

4.2.1 1c-MTV Results

The 1c-MTV measurements provide an estimate of the streamwise component of the total velocity field. This estimate of u, corresponding to the cases of $g' \sim 25$ mm$/s^2$ and $g' \sim 40$ mm$/s^2$, is shown as a space-time diagram in figures 4.5 and 4.6 respectively. As expected, the magnitude of velocities corresponding to a larger reduced gravity, g', are larger. This is also evident by the time of arrival of the gravity current, i.e. about 20 seconds for the case of $g' \sim 25$ mm/s^2 and about 16 seconds for $g' \sim 40$ mm/s^2. To demonstrate the quality of these measurements, instantaneous velocity profiles for the case of higher g' are presented in figure 4.7. Corresponding to the initial time when a stationary flow condition is expected (blue line in figure 4.7), we report an error in the measured streamwise velocity of the order of 0.3 mm/s. An estimate of the advection velocity of the gravity current can be made using the red line in figure 4.7. This estimate agrees well with the one obtained through the dye visualization experiments.

Ensemble averaging across all experiments of a fixed g' yields a velocity distribution as shown in figure 4.8. A time window of 3 seconds was used for this averaging. Here, the blue line represents the initial conditions of flow stationarity inside the FOV. The gravity current arrives subsequently, introducing a mean shear along with it (see yellow line in figure 4.8a and red line in figure 4.8b). As the current head passes by, the magnitude of this shear decreases gradually, as can be observed from the profiles at later times.

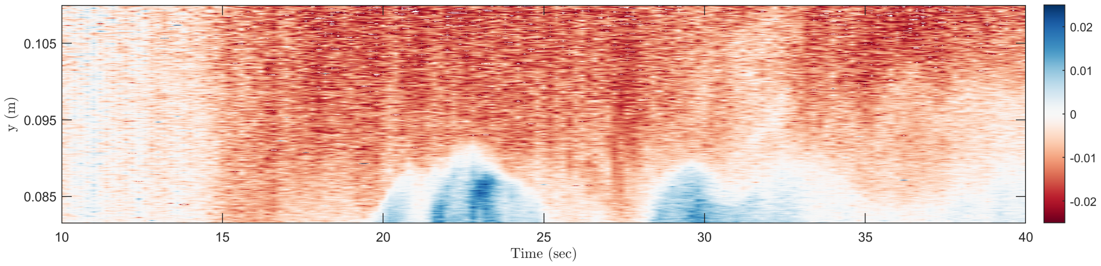

FIGURE 4.5: Temporal development of streamwise component of instantaneous velocity, u. $g' \sim 25$ mm/s^2

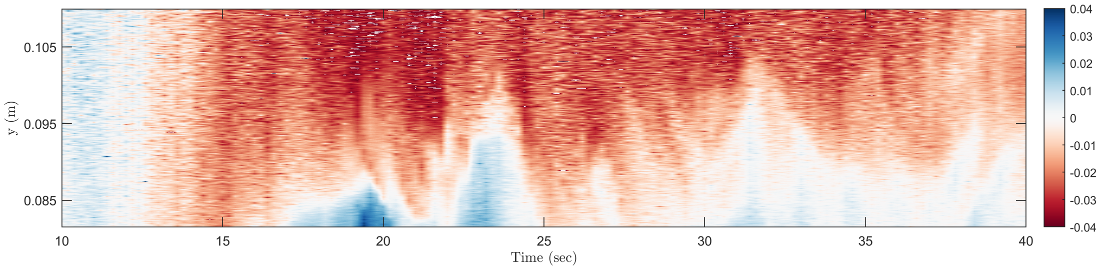

FIGURE 4.6: Temporal development of streamwise component of instantaneous velocity, u. $g' \sim 40$ mm/s^2

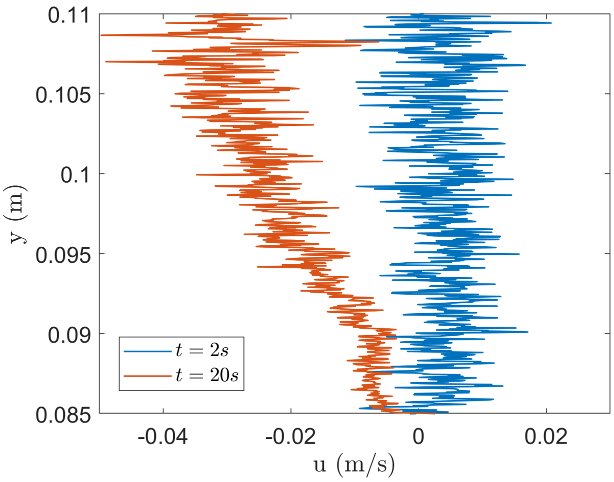

FIGURE 4.7: Instantaneous streamwise velocity estimates at an initial time (blue) and when the gravity current resides in the FOV (red).

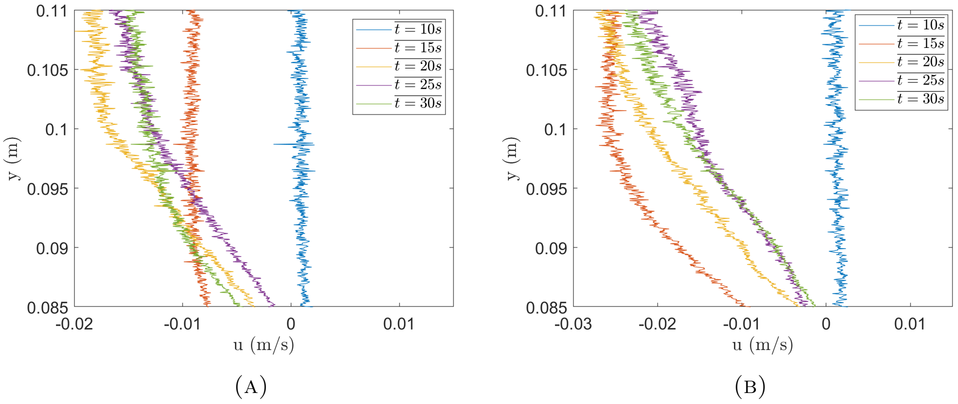

(A) (B)

FIGURE 4.8: Development of average velocity distribution for the case of (A) $g' \sim 25$ mm/s^2 and (B) $g' \sim 40$ mm/s^2. A 3 seconds time window was used from individual experiments in this averaging.

4.2.2 MTT Results

The simultaneous estimates of fluid temperature (along with the velocity) for the two cases are presented in the form of space-time diagrams in figures 4.9 and 4.10. One can observe that only the hot fluid prevails in the FOV until the gravity current arrival. This is followed by a gradual dilution of the current, as qualitatively evident from the reduced contrast of these plots. Similar to the previous discussion, instantaneous temperature profiles for the case of $g' \sim 40$ mm/s^2 are presented in figure 4.11. The error associated with the measured temperature was estimated as $\pm$ 0.25 ^{o} C. This can also be observed as small fluctuations in the temperature signal at an initial time (see the blue line in figure 4.11). On the other hand, the interface of the gravity current results in a rapid change in measured temperature in the direction normal to the current propagation, as suggested by the red line.

For further analysis, the density distribution was obtained from these temperature measurements using the correlation provided by Wexler and Hyland [69]. We use the fluid densities at the start of an experiment, ρ_H and ρ_C, to normalize the density field as

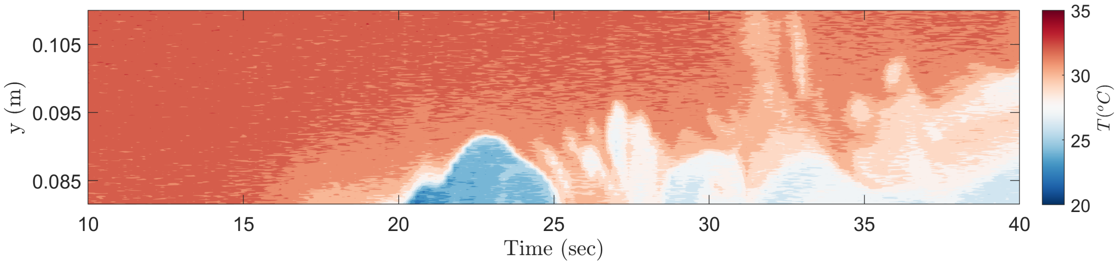

FIGURE 4.9: Temporal development of the fluid temperature, T as measured using MTT, $g' \sim 25$ mm/s^2.

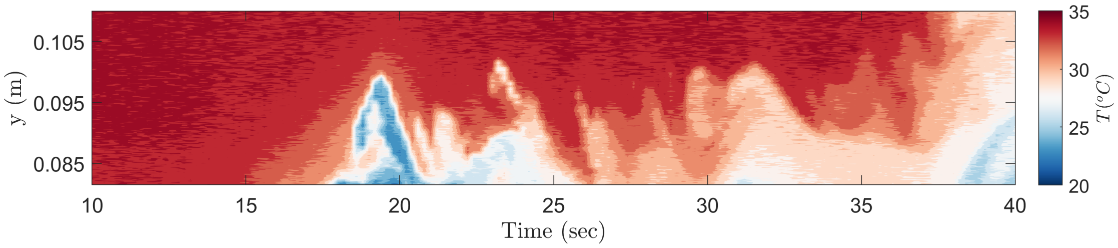

FIGURE 4.10: Temporal development of the fluid temperature, T as measured using MTT, $g' \sim 40$ mm/s^2.

$$\rho' = \frac{\rho - \rho_H}{\rho_C - \rho_H}, \tag{4.1}$$

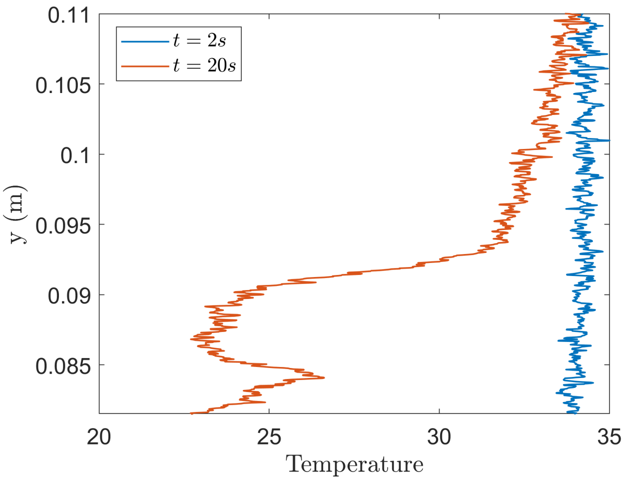

FIGURE 4.11: Instantaneous temperature profiles at an initial time (blue) and when the gravity current resides in the FOV (red).

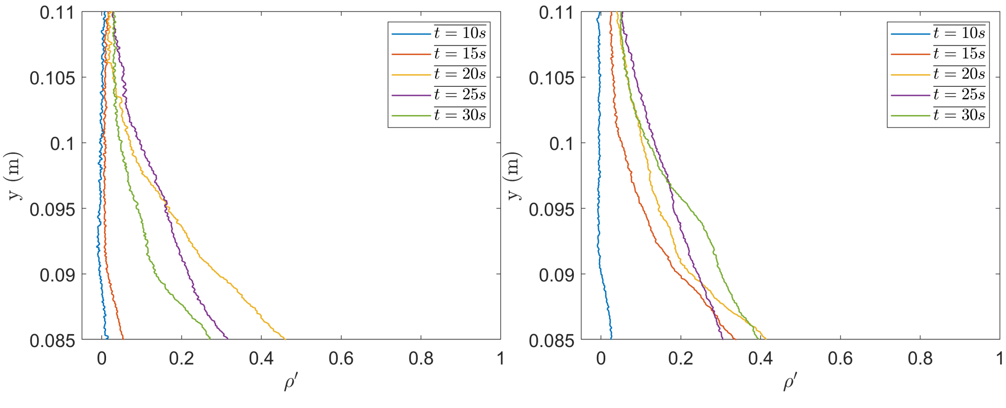

(A) (B)

FIGURE 4.12: Development of normalised density for the case of (A) $g' \sim 25$ mm/s^2 and (B) $g' \sim 40$ mm/s^2.

where ρ is the measured density. While a value of $\rho' = 1$ represents the cold fluid, $\rho' = 0$ corresponds to the hot fluid density at the start of an experiment.

Ensemble averaging across all the experiments of fixed g' results in a dimensionless density distribution as shown in figure 4.12. Similar to the previous analysis, an averaging window of 3 seconds was used to obtain these ensembles. Initially, the presence of hot fluid inside the FOV is marked using the blue line ($\rho' \approx 0$). Density gradients are subsequently introduced as a result of sharp temperature differences across the interface. Due to mixing between the two fluids, however, the magnitude of these gradients reduce with time.

4.2.3 Interfacial properties

The spatial resolution offered by the 1c-MTV/MTT measurements allowed detailed measurements of streamwise velocity and density across the interface, that are now presented. In order to calculate these properties, the vertical location of the interface within the FOV was first sought. This was obtained by putting a threshold on the measured dimensionless density estimates, ρ'. A threshold of 0.4 was found by locating the plateau in the probability density function (p.d.f.) of ρ' as shown in figure 4.13 [70]. The detected interface, overlaid on the density contours, is shown in figure 4.14. Due to the transient nature of the flow and the limited FOV, the interface was not detected at all times (see figure 4.14a, 25 s < t < 28 s and figure 4.14b, 26 s < t < 30 s). The properties presented next, therefore, correspond to the times when the interface was observed in the FOV.

After locating the interface, estimates of the local density and streamwise velocity were

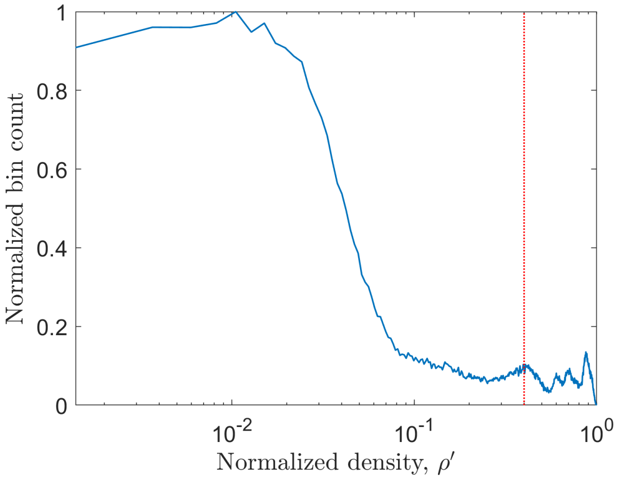

FIGURE 4.13: Distribution of normalized density, ρ', for the case of a $g' \sim 40$ mm/s^2 experiment.

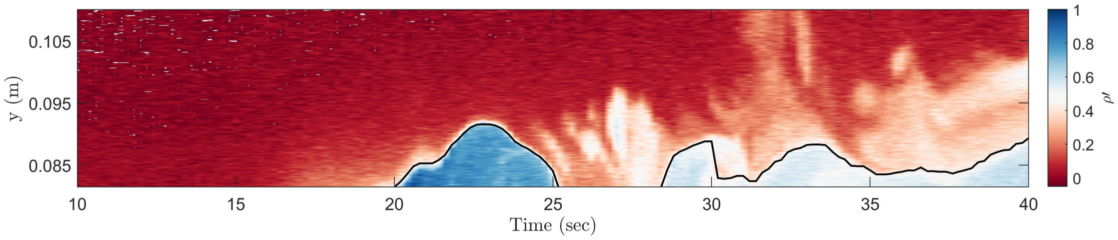

(A)

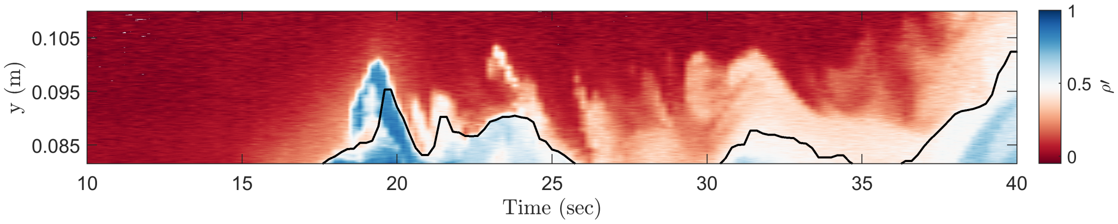

(B)

FIGURE 4.14: Density interface, shown as black, overlaid on the density space-time contours for (A) $g' \sim 25$ mm/s^2 and (B) $g' \sim 40$ mm/s^2.

obtained for 150 points on either sides of the interface. This corresponds to a vertical span of approximately 8 mm. A temporal average over a window size of 1 sec was used to remove small-scale noise in the instantaneous profiles. For the two g' considered, the calculated interfacial properties are shown in figures 4.15 and 4.16. In these plots, the vertical distance from the interface has been normalized using the tank height, H.

From figure 4.15a and 4.16a, a sharp density gradient was observed at the interface once the gravity current enters the FOV. The relative magnitude of this gradient was larger for the lower g' experiment. The two fluids across the interface subsequently mix together resulting in smaller density gradients, as evident at later times. This interfacial

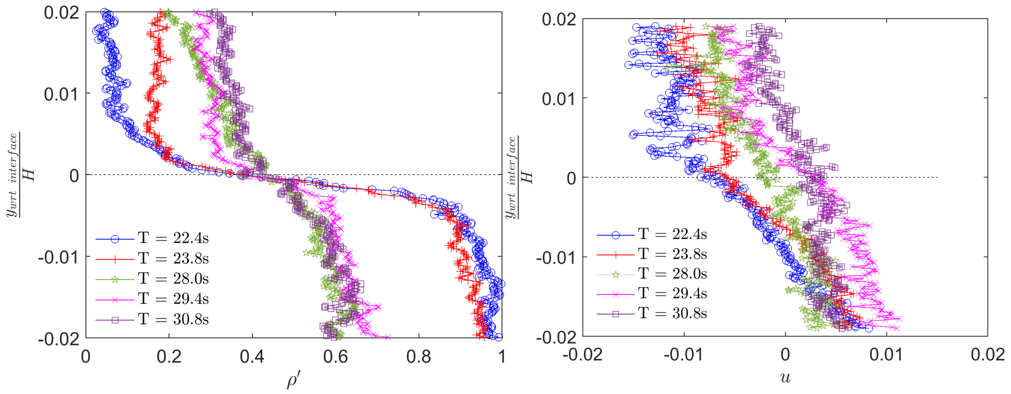

(A)

(B)

Figure 4.15: Development of (A) density and (B) streamwise velocity at the interface for the case of $g' \sim 25$ mm/s^2.

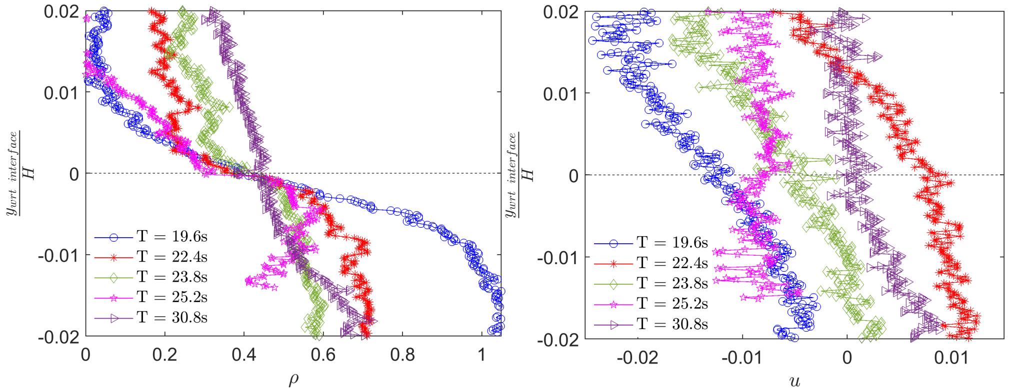

(A)

(B)

Figure 4.16: Development of (A) density and (B) streamwise velocity at the interface for the case of $g' \sim 40$ mm/s^2.

mixing is analyzed in detail in subsequent sections. Due to limited development length for the gravity current, we do not observe any further flow dilution. A similar trend can also be observed for the interfacial streamwise velocity profiles plotted in figure 4.15b and 4.16b. Albeit less apparent, the magnitude of shear at the interface decays with time.

4.3 Mixing efficiency

Mixing efficiency estimates for the present lock exchange flow are now presented and discussed. To accomplish this, the variation of background potential energy, $\mathcal{P}_B$, within the measurement field of view is first calculated. The primary focus of the present study is to quantify the *irreversible* mixing. Since, there exists a direct connection between the rate of change of background potential energy, $\frac{d\mathcal{P}_B}{dt}$, and the associated irreversible mixing [23, 26, 33], it is important to estimate $\mathcal{P}_B$ and its rate of change, $\frac{d\mathcal{P}_B}{dt}$, accurately. Typically, accurate estimates of $\mathcal{P}_B$ require the entire three-dimensional density field [22, 23, 57], which are generally available only from numerical simulations. Therefore, the analysis adopted in the present study is based on assumptions and approximations that are discussed and evaluated later.

After obtaining the estimates for the changes in background potential energy, $\frac{d\mathcal{P}_B}{dt}$, we quantify the instantaneous mixing rate, $\mathcal{M}$, see (1.23). To the best of the author's knowledge, this study presents the first experimental estimates of $\mathcal{M}$ in a thermally stratified lock-exchange flow. Physically, $\mathcal{M}$ represents the mixing that results in a permanent change in fluid properties *due to fluid motion.* Therefore, the present analysis eliminates the contributions from diffusive processes that could also result in similar permanent changes.

Finally, mixing efficiency is obtained by comparing the relative magnitudes of $\mathcal{M}$ against the viscous dissipation, ϵ. The estimates of cumulative mixing efficiency (see (1.28)) are presented first. The findings of this study are then compared with the estimates available in the literature. The shortcomings associated with the present experimentation are also discussed. Next, the variations in the instantaneous mixing efficiency, ε_i, (see (1.27)) are presented. A direct connection between the localized values of high ε_i due to coherent vortical stirring and consequently a delayed peak in mixing efficiency is found, which would be discussed towards the end of this chapter.

4.3.1 Evolution of background potential energy

To calculate the background potential energy, $\mathcal{P}_B$, of the flow, instantaneous density profiles obtained through the MTT measurements are re-arranged or 'sorted' such that the resulting density distribution yields a stable stratification. Therefore, the sorting algorithm places the heaviest/lightest fluid element on the bottom/top in the measurement FOV. An example of such an rearrangement is shown in figure 4.17. $\mathcal{P}_B$ is the potential energy associated with this sorted density profile and was calculated according to (1.21).

The time evolution of the background potential energy, $\mathcal{P}_B$, for the two cases is shown in figure 4.18. As expected, before the gravity current enters the field of view, the

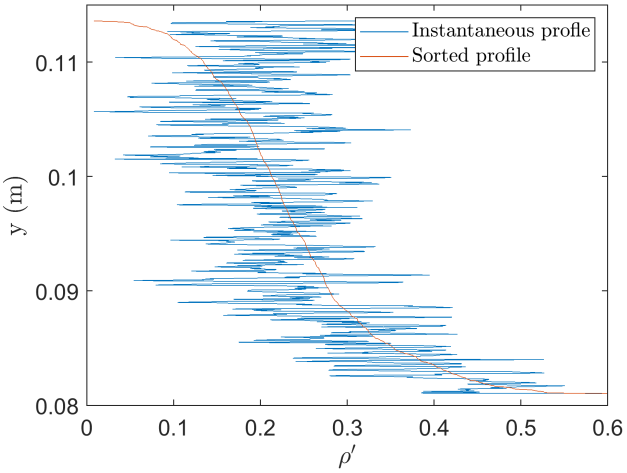

FIGURE 4.17: Instantaneous normalised density profiles at any time (blue) and the corresponding adiabatically stably stratified 'sorted' density profile (red).

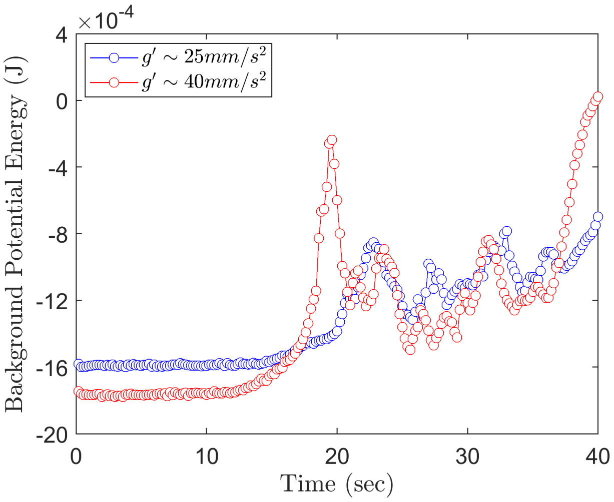

FIGURE 4.18: Variation of the background potential energy with time

lower g' has higher $\mathcal{P}_B$ compared to the higher g' case. Initially, both the flow fields possess minimum $\mathcal{P}_B$ and a sharp increase is observed as the gravity current enters the measurement FOV. This sudden increase is a result of the cold (dense) fluid contained in the gravity current entering the measurement domain thereby resulting in a higher potential energy. After the current head passes, the variations in $\mathcal{P}_B$ are observed to be more chaotic. This could be a result of the fluctuations in the vertical location of the interface within the measurement control volume. Another, more important reason behind this variation is the exchange of mass and momentum across the control volume boundaries that could change the instantaneous value of $\mathcal{P}_B$ (see (1.23)).

Based on the discussions in sections 1.2.1.3 and 1.3, we have established that the rate of change of $\mathcal{P}_B$, $\frac{d\mathcal{P}_B}{dt}$, plays an important role to quantify mixing in stratified flows. In the present study, we evaluate $\frac{d\mathcal{P}_B}{dt}$ in two different ways that are now discussed.

First, the quantity $\frac{d\mathcal{P}_B}{dt}$ corresponds to the temporal derivative associated with figure 4.18 or equivalently taking direct time derivative of (1.21). However, theoretically, the same quantity can also be calculated by employing the R.H.S. of (1.23). The latter involves estimation of the advective and diffusive fluxes that could be transferred across the bounding surface of the control volume, and the diapycnal mixing term, ϕ_d. The usage of either of these approaches require assumptions due to the limitations associated with the present measurements. These assumptions are now stated and discussed.

The present measurements provide the density field and the streamwise component of velocity along a vertical line, both at high spatial resolution. Therefore, to calculate $\frac{d\mathcal{P}_B}{dt}$ using the second approach, we only consider the contributions from streamwise velocity, u, to estimate the advective flux in (1.23). The fluxes due to the wall-normal velocity, v, and the wall-parallel velocity, w, are neglected. From the continuity analysis, we found that v is at least one order magnitude smaller than u. This estimate is in accordance with the previous entrainment study of Balasubramanian and Zhong [21] who measured v/u to be about 0.05. Therefore, the inclusion of only the streamwise component of velocity should provide reasonable estimates of the advective fluxes. The quantification of diffusive flux and the diapycnal mixing, ϕ_d, in (1.23) requires a three-dimensional density field. However, due to the nature of the data in the present analysis, we neglect the density variations in streamwise (x) and spanwise (z) directions. The assumption is partially justifiable because of the predominantly uni-directional variations that exist in the flow. The temperature (density) gradients associated with these counter-travelling gravity currents are primarily normal to the flow direction.

To explore the reasonableness of these approximations, we first calculated the rate of change of $\mathcal{P}_B$ by taking the direct temporal derivative of $\mathcal{P}_B$ (using (1.21) and essentially through figure 4.18). This is then compared to the right- hand side of (1.23) that contains the contributions from advection, diffusion and diapycnal mixing. Theoretically, the two approaches should yield an identical result. With the simplifications mentioned above, the comparison between the results of the two approaches is shown in figure 4.19. As is apparent, the agreement justifies the reasonable use of the noted approximation. Based on this validation, the further analysis involves estimation of the instantaneous mixing rate, $\mathcal{M}$, through the diapycnal mixing rate, ϕ_d, as discussed next.

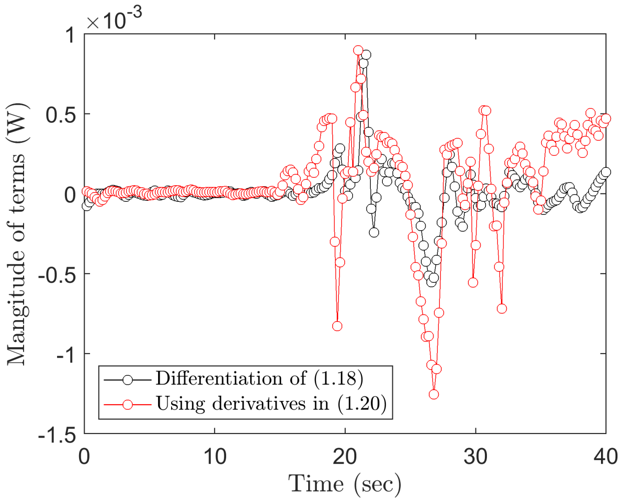

FIGURE 4.19: Rate of change of $\mathcal{P}_B$, $\frac{d\mathcal{P}_B}{dt}$, calculated the time-derivative of (1.21) (black) and by summing the fluxes involved in (1.23) (red), $g' \sim 40$ mm/s^2.

4.3.2 Cumulative mixing efficiency

The estimate of cumulative mixing efficiency, ε_c, for the thermally driven lock-exchange flow is now presented. The analysis used in the present study requires a time series for the instantaneous mixing rate, $\mathcal{M}$, and the viscous dissipation, ϵ for the quantification of ε_c (see equation 1.27). The instantaneous mixing rate was obtained from the estimates of diapycnal mixing term, ϕ_d, (evaluated in the previous section) and a diffusion term, ϕ_i, as

$$\mathcal{M} = \phi_d - \phi_i.$$

Physically, ϕ_i represents the diffusive processes that could result in permanent changes in fluid properties owing to small-scale diffusion. The magnitude of ϕ_i is negligible (compared to ϕ_d) for a turbulent flow and is only meaningful for laminar flows [24]. However, the gravity currents produced by the present experiments are in the moderate Reynolds number range ($Re < \mathcal{O}(10^4)$), i.e. not highly turbulent. Therefore, an analysis is required to verify the relative magnitudes of ϕ_d and ϕ_i. For the two experimental cases, this comparison is shown in figure 4.20. As the plots suggest, the relative contribution of the diffusive component, ϕ_i, is much smaller than the total diapycnal mixing, ϕ_d. Consequently, the contributions to $\mathcal{M}$ comes primarily from ϕ_d. This implies that the diffusive conversion of internal energy towards an increment in $\mathcal{P}_B$ is minimal, and majority of the changes in the background potential energy of the flow are due to the kinetic energy of the flow (see figure 1.4).

Using the procedure detailed in section 3.2.3, the viscous dissipation, ϵ, was obtained

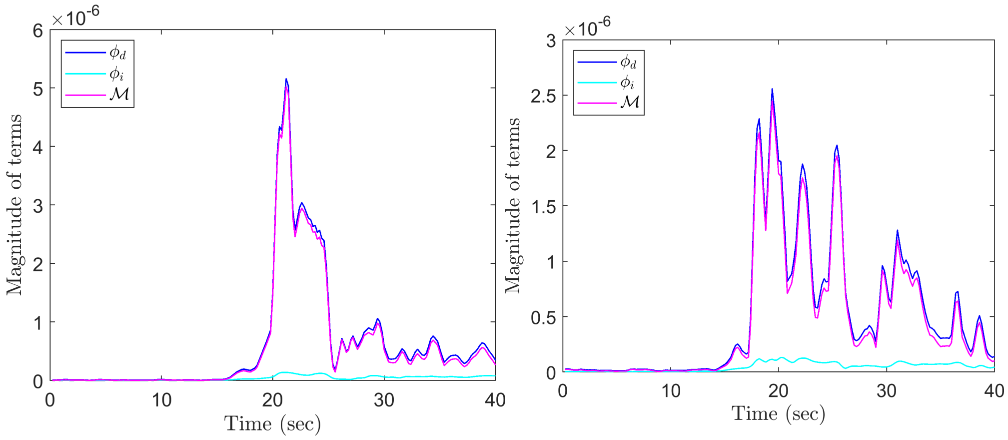

(A)

(B)

FIGURE 4.20: The magnitude of various terms associated with the stratified mixing for the case of (A) $g' \sim 25$ mm/s^2 and (B) $g' \sim 40$ mm/s^2.

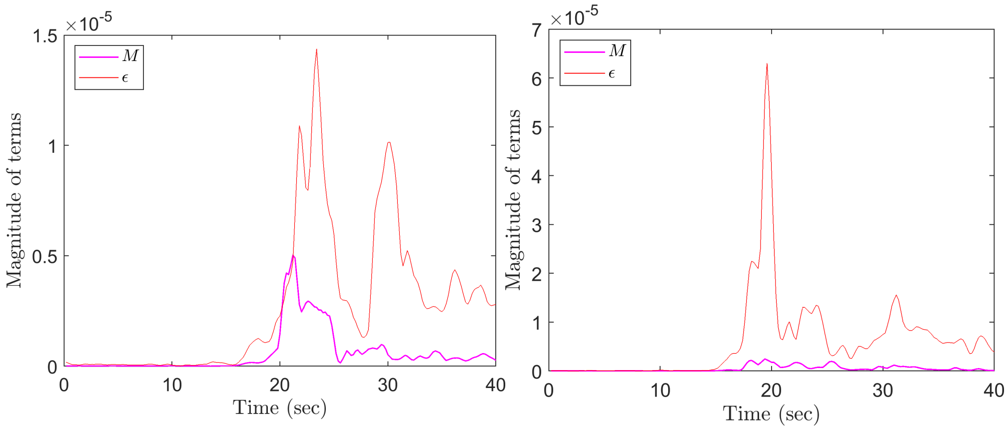

(A)

(B)

FIGURE 4.21: Estimates of mixing rate, $\mathcal{M}$, and viscous dissipation, ϵ, for the case of (A) $g' \sim 25$ mm/s^2 and (B) $g' \sim 40$ mm/s^2.

through employing the isotopic estimate. This approximation is also supported by the numerical study of Hebert and de Bruyn Kops [71] who suggested that the vertical gradients could contribute upto 90% towards the dissipative processes in stratified flows. The experimental estimates of ϵ from the present study, along with the instantaneous mixing rate, $\mathcal{M}$, are shown in figure 4.21. As expected, the interfacial dissipation is larger for the case of higher g'. However, we also observe that the maximum value of dissipation obtained for experiments at fixed g' varied by up to 20%. This variation is attributed to the transient nature of the flow and a limited measurement domain. The resulting impact on the mixing efficiency due to this run-to-run variability in $\mathcal{M}$ and ϵ for experiments at fixed g' is discussed now.

Figure 4.22 presents a scatter plot showing the variation of cumulative mixing efficiency,

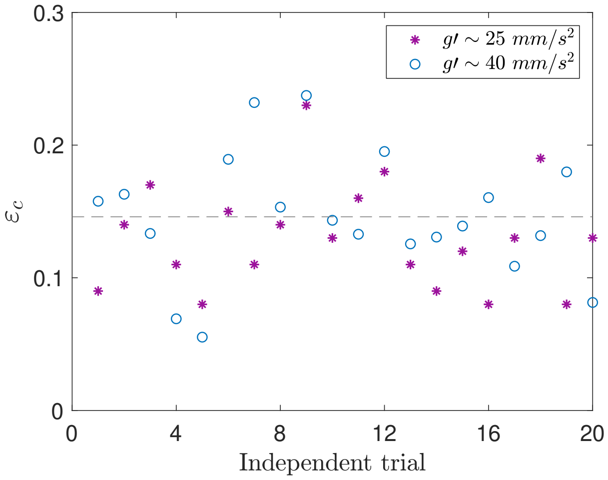

FIGURE 4.22: Calculated values of cumulative mixing efficiency, ε_c, for all the measurements. Horizontal line represents the average value.

$g'(mm/s^2)$	$\overline{\varepsilon_c}$
~ 25	0.13
~ 40	0.14

TABLE 4.1: Estimates of cumulative mixing efficiency calculated using 1c-MTV/MTT for a lock-exchange flow.

ε_c, for all of the experiments. The integration involved with these calculations (see (1.28)) used the gravity current arrival time inside the FOV as $t = 0$. The integration was performed up to the time instant when the gravity current hits the end-wall of the facility. The run-to-run variability is apparent in the data scatter. No net bias is evident in these estimates of the cumulative mixing efficiency, and the standard deviation of ε_c over these 40 runs is 0.05.

The average values of cumulative mixing efficiency, $\overline{\varepsilon_c}$, are reported in table 4.1. These values are now compared with the estimates of mixing efficiency previously reported in the literature. The benchmark study of Osborn [28] suggested a canonical value of $\Gamma \sim 0.2$. Their definition was, however, based on the buoyancy flux, ϕ_z, and therefore, does not solely account for irreversible mixing. To the author's knowledge, direct estimates of irreversible mixing efficiency have only been obtained through the numerical simulations, e.g. such as by Ilicak [59]. He reported that the mixing efficiency, ε_c, is a function of the Reynolds number and concluded that ε_c saturates at 0.12 for $Re > 2500$. Regarding experimental estimates, the closest approach in quantifying mixing efficiency in this configuration of lock-exchange experiment was carried out by Hughes and Linden [64]. Using the initial and final potential energies, PE_i and PE_f, they obtained the total increment in the potential energy and compared it to the available potential energy in the flow. Based on this, they reported an asymptotic value of mixing efficiency as 0.08. Compared to these estimates, the average value of mixing efficiency obtained in the present study is slightly higher, although of a similar magnitude. Importantly, however, we should mention that the definition of mixing efficiency used by Hughes and Linden [64] is not the same as the one used here.

One of the major restrictions inherent to the present experiments is the measurement field of view. Generally, the experimental studies investigating mixing in a lock-exchange flow (irrespective of their definition of mixing efficiency), e.g. Hacker et al. [31], Fragoso et al. [72] and Balasubramanian and Zhong [21], employ a planar measurement section that spans approximately half the total length of the facility. In comparison, the present measurements utilize a relatively narrow measurement domain which, although focused at the interface between the gravity currents, spanned only a fraction of the total length of the facility. Also, the extent up to which these estimates of ε_c are affected by the size of measurement domain is yet to be fully characterized.

4.3.3 Instantaneous mixing efficiency and the mechanisms of efficient mixing

The variation in the instantaneous mixing efficiency, ε_i, obtained through the present measurements are now presented. As described below, the behaviours of ε_i provides a basis for understanding the instantaneous flow mechanisms that contribute towards efficient mixing.

The range of values over which the instantaneous mixing efficiency spans across all the experiments is shown through a joint probability distribution between the instantaneous mixing rate, $\mathcal{M}$, and the viscous dissipation, ϵ, in figure 4.23. Lines of constant ε_i are overlaid on top to highlight this scatter. Corresponding to the empirical observation of Osborn [28], our measurements suggest that up to 75% of mixing efficiency values are below 0.2. This plot also depicts the situations where higher values of instantaneous mixing efficiency, beyond the canonical estimate of 0.2, are observed. The events that lead to such high values are the main focus of this section.

Figure 4.24 presents the procedure to quantify the time-evolution of instantaneous mixing efficiency for the case of $g' \sim 40$ mm$/s^2$. After obtaining the instantaneous mixing

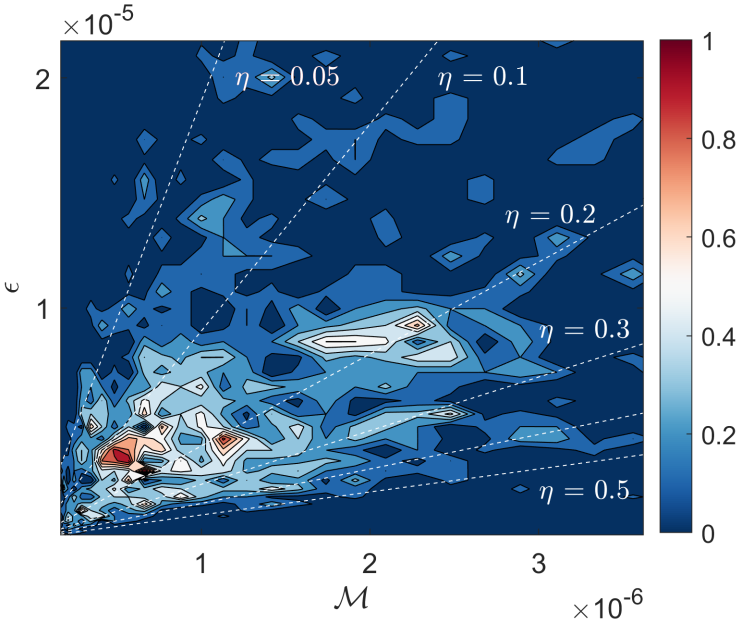

FIGURE 4.23: Joint probability distribution between the instantaneous mixing rate, $\mathcal{M}$, and the viscous dissipation, ϵ, with lines of constant mixing efficiency overlaid on top.

rate, $\mathcal{M}$, and the viscous dissipation, ϵ, the instantaneous mixing efficiency, ε_i, is obtained using (1.27). Since the magnitude of $\mathcal{M}$ and ϵ is nearly zero for $t \leq 15$ s, the instantaneous mixing efficiency, ε_i, prior to this time is not meaningful and therefore, is not considered in the calculation of ε_c as mentioned previously. The variation of ε_i for the case of a random $g' \sim 25$ mm$/s^2$ experiment, along with the $g' \sim 40$ mm$/s^2$ case, is shown in figure 4.25.

A closer look at figure 4.25 reveals a local maxima in the ε_i at $t \simeq 28$ s for the case of $g' \sim 25$ mm$/s^2$ while two distinct peaks were found for $g' \sim 40$ mm$/s^2$ at the 23 second and 25 second marks respectively. To investigate these regions of high instantaneous mixing efficiency, we revisit the flow visualization data provided by the *DV2* experiments. Recalling that these visualizations provide a qualitative way to identify the location of certain characteristic flow features such as vortical overturns. Using these visualizations, the *signature* of such a feature in the space-time contour of dye intensity is marked as a red box in figure 4.26a. Since, the 1c-MTV/MTT experiments do not provide a direct visualization platform, the signatures obtained through the dye visualization experiments are examined for characteristic flow features in the density space-time contours of the 1c-MTV/MTT measurements. This allows us to locate the presence of vortical features in our measurement, and are shown as black boxes in figure 4.26b and 4.26c. The mixing implication of these flow features and their quantitative

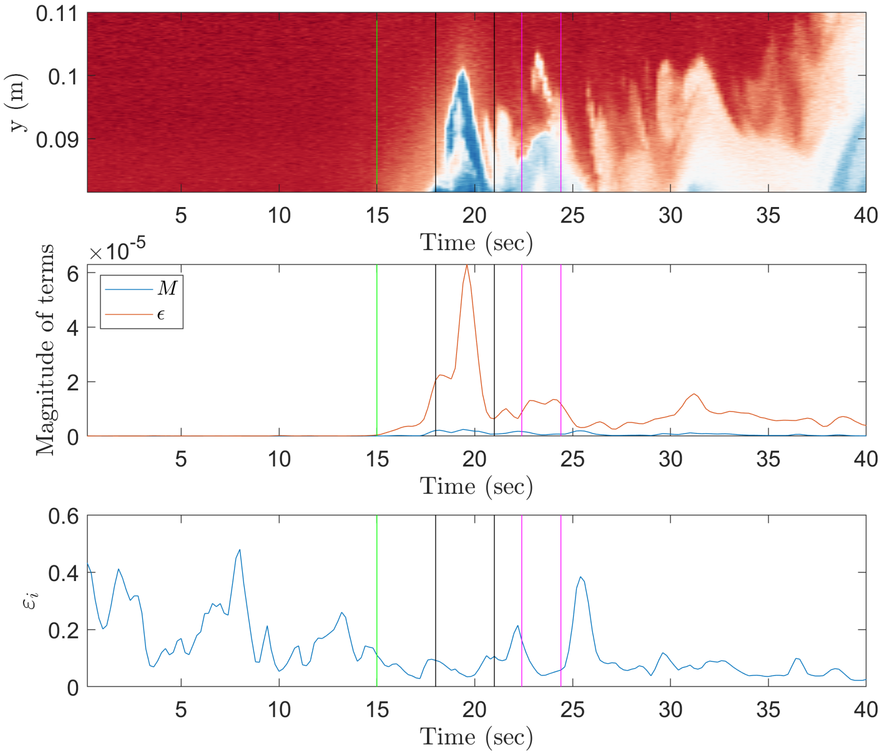

FIGURE 4.24: Representation of the density contour (top) and the corresponding variation of $\mathcal{M}$ and ϵ (middle) for the case of $g' \sim 40$ mm/s^2. This yields the instantaneous mixing efficiency (bottom). The flow events are occurring between the vertical black and magenta lines while the green line represents the time when the gravity current enters FOV.

attributes are now discussed.

Figure 4.24 also presents a systematic approach to evaluate the qualitative and quantitative effects of the noted flow features. For the cases of $g' \sim 40$ mm/s^2, their corresponding temporal span in the density space-time contour (top) is marked using black and magenta lines. The associated variations in the instantaneous mixing rate, $\mathcal{M}$, and the viscous dissipation, ϵ, are also shown (middle figure). We observed relatively higher dissipation during the event and as a consequence, the instantaneous mixing efficiency, ε_i, as shown on the bottom, attenuates. An interesting observation here, however, is that the peak value in the ε_i occurs *after* the occurrence of these high dissipation events. A similar behaviour, although not shown, was observed for the case of $g' \sim 25$ mm/s^2. It is not unreasonable to expect that the local gradients are high during a vortical overturn for instance, that enhances the dissipation and hence suppresses the ε_i temporarily. However, after such an event has passed, the resultant flow field possess low values of

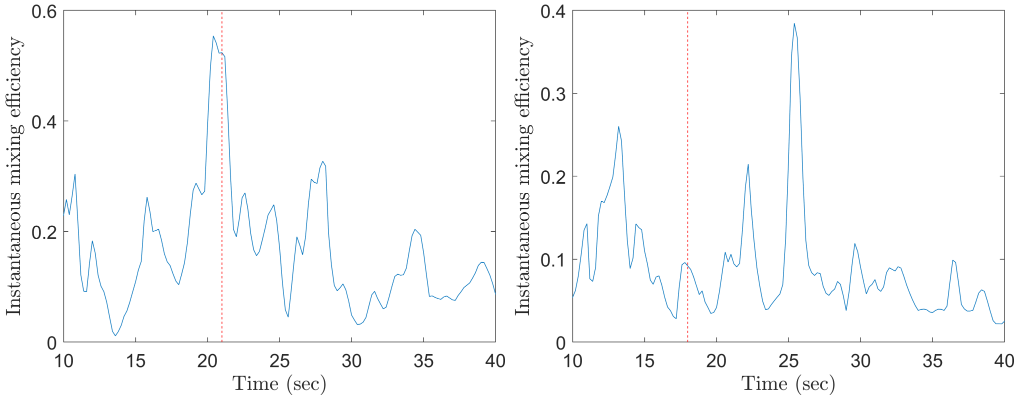

(A) (B)

FIGURE 4.25: The variations in the instantaneous mixing efficiency, ε_i, for the case of $g' \sim 25$ mm$/s^2$ (A) and $g' \sim 40$ mm$/s^2$ (B). Vertical red line denotes the front arrival time within the FOV.

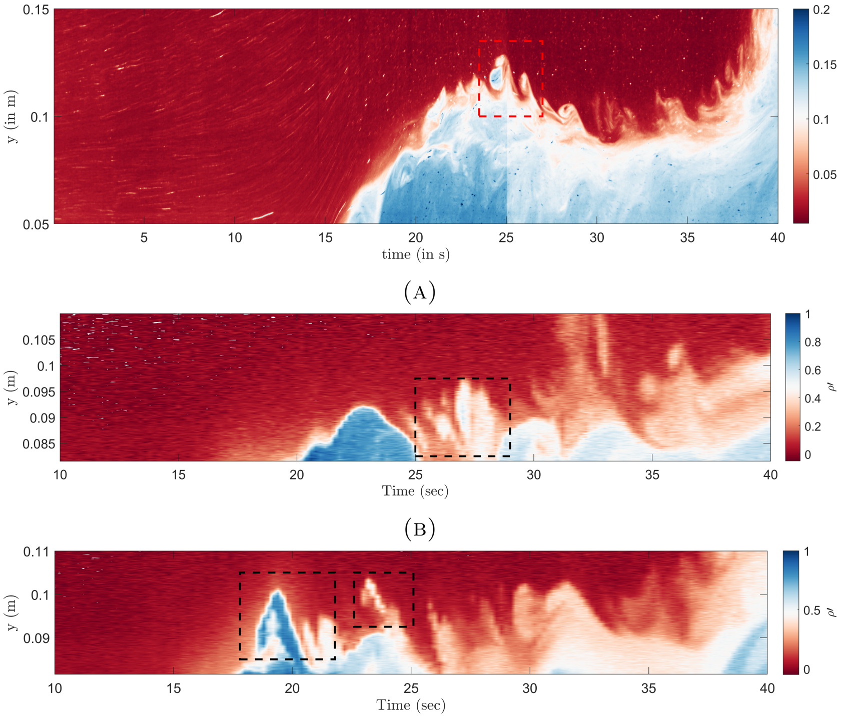

(A)

(B)

(C)

FIGURE 4.26: (A) Space-time diagram of the fluorescein dye intensity from a *DV2* experiment. Red box indicates the occurrence of a vortical overturn. (B) and (C) plots the variation of non-dimensional density, ρ', for the cases of $g' \sim 25$ mm$/s^2$ and $g' \sim 40$ mm$/s^2$ respectively. Black boxes locate the signature observed in 4.26a.

flow gradients (i.e. lower dissipation) suggesting higher instantaneous mixing efficiency. Notice that after the flow events pass, the value of instantaneous mixing rate, $\mathcal{M}$, is also higher contributing to a higher ε_i. Therefore, it is reasonable to suggest that the fluid elements that are stretched and increased in area (due to vortical events accompanied by high dissipation and low ε_i) are subsequently contributing more towards irreversible mixing ($\mathcal{M}$) and hence increased ε_i. The contributions of these events suggests that the overall mixing in a lock-exchange flow flow is largely determined by their occurrence. This behaviour was also reported in the PIV-PLIF study of Balasubramanian and Zhong [21] who observed higher values of entrainment coefficient whenever a fluid roll-up occurred at the interface. Figure 4.24 also suggests that typically, such events are short-lived i.e. of the order of a few seconds, and importantly that increased ε_i happens *after* the overturn event.

Based on these observations, we conclude that while such localised events contribute significantly towards a higher mixing efficiency in a thermally driven lock-exchange flow; however, the changes they bring out in the instantaneous mixing efficiency are not immediate. Rather, there is a lag associated with their occurrence and the corresponding rise in the instantaneous mixing efficiency. The cartoon illustrated in figure 4.27 further describes the qualitative and quantitative behaviours that could be associated with such events. In this cartoon, we have taken the example of a vortical overturn advecting with the current. Not surprisingly, this is inspired by the flow behaviour observed in the dye visualization experiments. These overturns bring together fluid parcels of different densities that could potentially result in irreversible mixing. The middle row of this cartoon shows the corresponding instantaneous streamwise velocity and normalized density profiles from the 1c-MTV/MTT experiments. These profiles correspond to the time where the signatures of such events were located in the density space-time contour, as discussed previously. The last row plots the temporal variation of the instantaneous mixing efficiency, ε_i. Here, the time instants during and after the 'mixing event' are marked as A and B respectively. As evident from figure 4.27, the instantaneous velocity and density distributions during the event, as shown by the black box, produce large gradients in the flow (refer to figure 4.24).

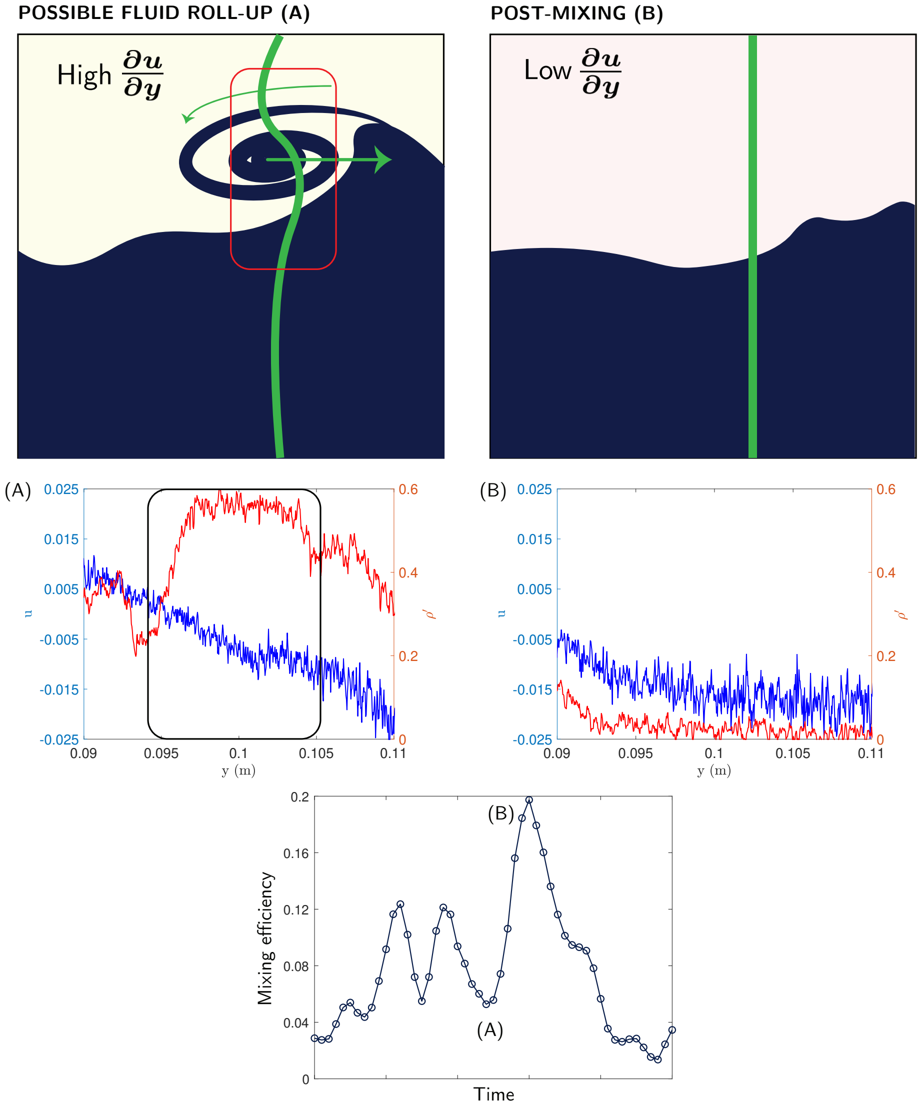

FIGURE 4.27: Cartoon illustrating a localized event that might result in a local maxima in the instantaneous mixing efficiency. Figures in the middle row presents the variation of streamwise velocity (blue) and density (red) during the event (A) and post-mixing (B).

Chapter 5

Summary and Conclusion

The main findings of the present work, specifically addressing the problems outlined in the first chapter, are now summarized:

- The measurement technique, 1c-MTV/MTT, was efficiently employed to obtain simultaneous measurement of streamwise velocity and temperature fields at the gravity current interface in a thermally stratified lock-exchange flow. These data were acquired along a line providing multi-point simultaneous measurements. The interfacial velocity was determined with an uncertainty of ± 0.3 cm/s whereas, the corresponding error in the measured temperature field was shown to be 0.25 degrees. These measurements, corresponding to every pixel location, were shown to resolve both the characteristic length scales of the flow i.e. Kolmogorov length scale for the velocity field and Batchelor scale for the scalar (temperature) field. Therefore, this study provided an experimental approach towards high-resolution multi-point simultaneous velocity and temperature measurements in a general flow field.

- The changes in the background potential energy were measured to estimate the diapycnal mixing rate. This, in turn, was used to quantify the extent of irreversible mixing that takes place between the two fluids that constitute the counter-travelling gravity currents. To the best of the author's knowledge, this study provided first experimental estimates of the irreversible mixing in a lock-exchange setup.

- The present measurements of velocity and temperature yielded an average cumulative mixing efficiency for the two experimental cases of $g' \sim 25$ mm$/s^2$ and $g' \sim 40$ mm$/s^2$ as 0.13 and 0.14, respectively. While the extent of measurement domain was limited in a spatial sense, these estimates of mixing efficiency were shown to be comparable (in order of magnitude) to the previously obtained values in a lock-exchange numerical simulations.

- Lastly, it was shown that occurrences of certain events in the flow e.g. vortical overturns, are linked to a high instantaneous mixing efficiency. The most noteworthy takeaway of this study is that these flow events occur *before* the peak in the mixing efficiency was observed. During such an overturn, high gradients in the flow were shown to provide a larger surface area available towards an enhanced molecular diffusion. Following this, the gradients diminish i.e. the fluid parcels mix together, resulting in a higher mixing efficiency.

5.1 Scope of future work

One of the limiting aspects of the present experimentation was a limited field of view. A larger FOV would not only allow to measure a larger cross-section in the flow, it would result in a better understanding of the instantaneous density field that forms the basis to evaluate the background potential energy. The cumulative mixing efficiency thus obtained would provide a better and fair estimate and comparison with other studies. Also, the driving mechanisms behind the high mixing efficiency events can be better understood with a larger spatial data set.

Since, the hot fluid temperature poses a restriction on the maximum allowable temperature difference between the two fluids in these lock-exchange experiments. Therefore, one way to obtain high Reynolds number gravity currents is to increase the height of the facility. The notion that mixing shall increase with higher Re, can thus be quantified in future.

Appendix A

Appendix A

A.1 Preliminary MTV Experiments in Channel Flow

With an overarching aim to validate the velocimetry technique, turbulent channel flow was studied using 1c-MTV. There is extensive experimental and numerical data available for the channel flow. These validation experiments were conducted in a rectangular water channel with test-section dimensions 60 mm × 750 mm × 9000 mm (H × W × L). These design aspect ratios were inspired after the works of Dean [73] and Monty [74] which suggested that to replicate the two-dimensional channel flow, the aspect ratio W/H should not be less than 7. Also, fully-developed turbulent flows can be expected as the development length exceeds $130H$. A schematic of the experimental facility is shown in figure A.1. Nine, one meter long sections were joined to form the test-section. Precision clamps joined the individual sections such that all interior surfaces were flushed. Before the flow entered the test-section, it passed through three screens, two with an open area of 72 %, and then one fine screen with an open area of 58 %. Following the screens, the flow passed through a contraction (indicated as C in the schematic) with an area reduction factor of 6.66. Fused silica optical windows installed flush into the channel

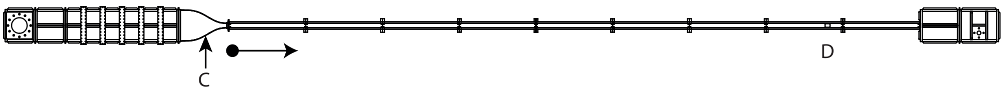

Figure A.1: Schematic of the water channel. C corresponds to the contraction before channel inlet while D located the measurement location.

floor and ceiling allow for laser beam access. Similarly, glass windows in the vertical side walls allow for camera viewing. These windows were located at 130H downstream of the contraction, as noted in figure A.2. The fluid flow was driven by a centrifugal pump that was controlled with a precision variable frequency drive.

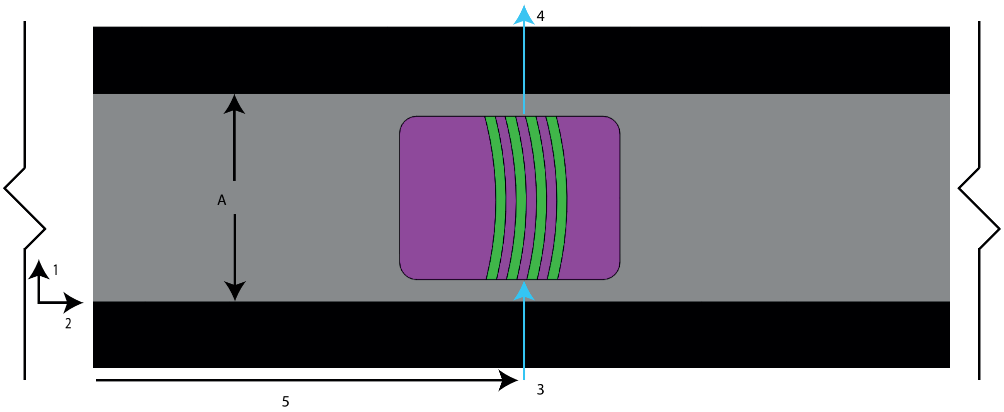

Figure A.2: Zoomed in view of the MTV portion of the facility. Flow is from left to right; green lines represent a typical set of deformed lines that constitute an MTV image.

Pressure was measured using a set of three differential pressure transducers located at different stations along the length of channel. Wall pressure taps, 1 mm in diameter, located at $x/H = 31.7$, 48.3 and 65 were used to measure the pressure while the downstream pressure port was located at $x/H = 131.7$. A linear curve-fit using these three Δp measurements as a function of length along the channel yielded pressure gradient. The temperature of fluid was measured using shielded T-type thermocouples at the inlet and outlet sections. Dynamic viscosity and fluid density as a function of fluid's temperature were obtained using the the relations provided by Nagashima [75] and Hyland and Wexler [65] respectively. The correlation between the friction velocity, u_τ and pressure gradient can easily be obtained using an integral momentum balance in the streamwise direction.

A.1.1 Velocimetry data validation

In this section, we aim to validate the obtained experimental statistics with that of the available direct numerical simulation (DNS) data. Particularly, through 1c-MTV, we measure high-resolution estimates of streamwise component of the total velocity field, u, which was then compared with the DNS datasets.

The measured streamwise velocity, u and wall-normal distance, y, was normalized using the friction velocity, u_τ, half-channel height, H and kinematic viscosity, ν. The experiments were conducted at four different Reynolds numbers, $\delta^+ = \frac{u_\tau \delta}{\nu}$, of approx. 360, 580, 850 and 1680. For these measurements, the comparison between the calculated inner-normalized mean velocity profiles and the DNS data of [7, 8] is shown in figure A.3.

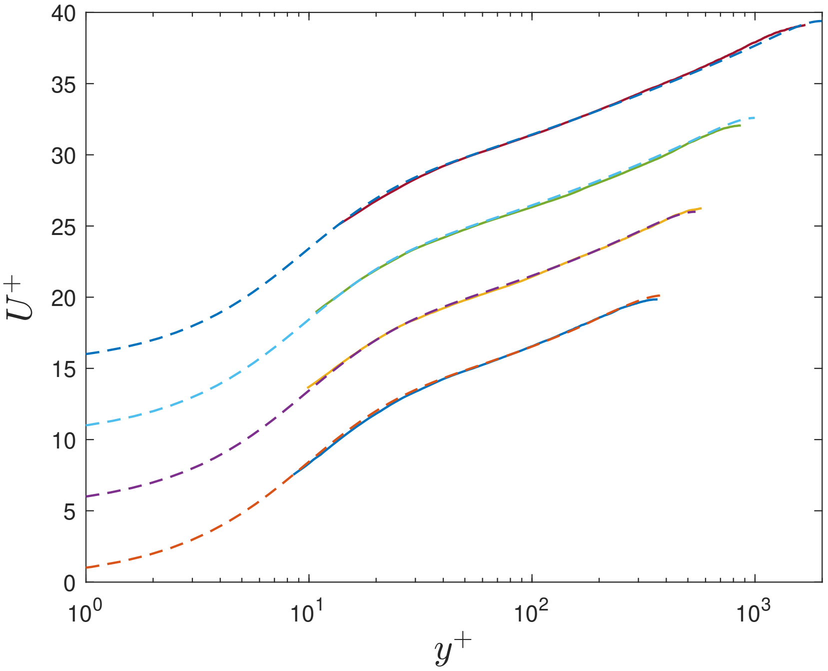

FIGURE A.3: Inner normalized mean velocity profiles calculated experimentally (solid lines), compared against the DNS profiles (dashed lines) at approximately similar Reynolds numbers. Note that the profiles are shifted by 5 between each δ^+. DNS datasets are from Moser et al. [7] and Lee et al. [8]. Proceeding from bottom to top, DNS/Exp. δ^+ values are 395/360, 550/580, 1000/850 and 2000/1680 respectively.

.

In general, the experimental results show excellent agreement with the DNS data for $y^+ \geq 12$ for the highest Reynolds number case. These instantaneous profiles contain about 875 data point, which considerably exceeds the data-points density in any of the DNS profiles considered for figure A.3. However, unlike the DNS profile where the points are non-uniformly spaced, experimental data points are equispaced in wall-normal direction with a spacing of about 0.4 and 1.9 viscous units for $\delta^+ = 360$ and $\delta^+ = 1680$ respectively.

For sanity check, the RMS profiles of streamwise velocity are also presented. First, the RMS profile for $\delta^+ = 1680$ is illustrated in figure A.4 to address the effect of spatial attenuation. It can be observed that the peak in the experimental profile lies well below than that of the DNS profile. This loss in the energy is due to the spatial averaging effect that was corrected using the technique described by [9]. This attenuation is attributed to the depth of focus (DOF) of the lens since the MTV technique possess a finite spatial resolution in spanwise direction (similar to that of the hot-wire sensors). The line thickness in spanwise direction (full-width at half the maximum intensity) acts like a characteristic length associated with the *sensor*. For these experiments, this length was estimated to be around 0.6 mm. Once corrected, the results obtained using MTV agree quite well with the DNS profile as illustrated in figure A.4.

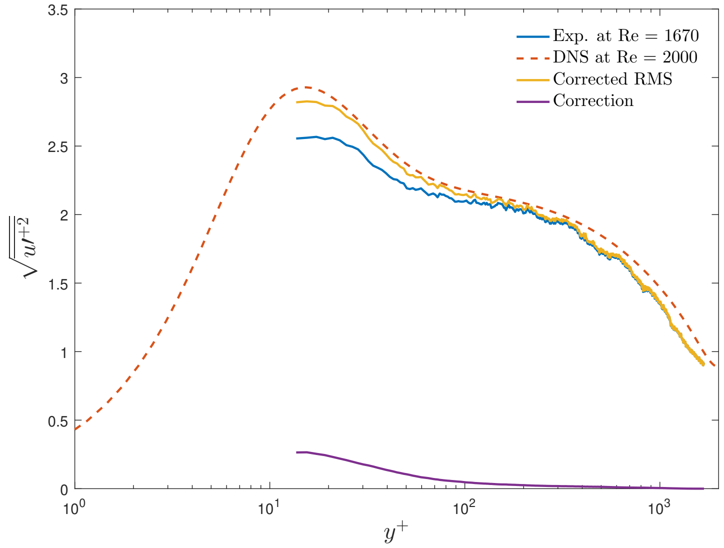

FIGURE A.4: Experimental RMS profile of streamwise velocity illustrating the effect of spatial attenuation at $\delta^+ = 1680$. Correction is calculated using the method proposed by [9]. The corrected profile is calculated by adding the correction to the experimental RMS profile.

.

The corrected experimental RMS profiles for all the Reynolds number studied are presented in figure A.5. These results appear to be in good agreement with the DNS data. For lower values of δ^+, experimental profiles yield a very close estimate because of negligible spatial attenuation. However, the peak RMS value for the higher δ^+ cases differ slightly from their DNS counterpart. Another possible reason behind this deviation is the difference in Reynolds number at which the two data sets are compared.

Although not presented here, but the mean derivatives of streamwise velocity, $\frac{\partial u}{\partial y}$ and $\frac{\partial^2 u}{\partial y^2}$, also agree well with the DNS data. These findings were reported by Elsnab et al.

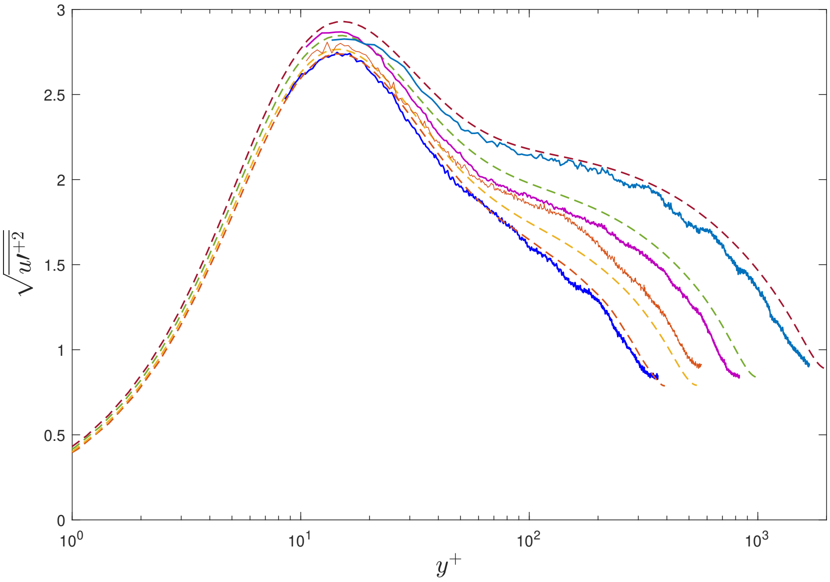

FIGURE A.5: Experimental RMS profile of streamwise velocity compared with the DNS data at various Reynolds number. The dashed line represents the DNS profile while the solid lines correspond to experimental datasets. Proceeding from left to right (beyond $y^+ = 100$), DNS/Exp. δ^+ values are 395/360, 550/580, 1000/850 and 2000/1680 respectively.

.

[47]. Based on these evidences, we qualify 1c-MTV as a well-suited technique to measure the velocity field for the lock-exchange experiments.

Bibliography

[1] T Brooke Benjamin. Gravity currents and related phenomena. *Journal of Fluid Mechanics*, 31(2):209–248, 1968.

[2] C P Gendrich, M M Koochesfahani, and D G Nocera. Molecular tagging velocimetry and other novel applications of a new phosphorescent supramolecule. *Experiments in Fluids*, 23:361–372, 1997. ISSN 0723-4864. doi: 10.1007/s003480050123.

[3] M M Koochesfahani and D G Nocera. Molecular tagging velocimetry. In *Handbook of experimental fluid dynamics*, pages 362–382. Springer-Verlag, 2007.

[4] H Hu and M. M. Koochesfahani. Molecular tagging velocimetry and thermometry and its application to the wake of a heated circular cylinder. *Measurement Science and Technology*, 17(6):1269, 2006.

[5] J. W. Rottman and J. E. Simpson. Gravity currents produced by instantaneous releases of a heavy fluid in a rectangular channel. *Journal of Fluid Mechanics*, 135: 95–110, 1983.

[6] J. O. Shin, S. B. Dalziel, and P. F. Linden. Gravity currents produced by lock exchange. *Journal of Fluid Mechanics*, 521:1–34, 2004.

[7] R D Moser and J Kim. Direct numerical simulation of turbulent channel flow up to Re 590. *Physics of Fluids*, 11(4):11–13, 1999.

[8] M Lee and R D Moser. Direct numerical simulation of turbulent channel flow up to Re_ tau approx 5200. *Journal of Fluid Mechanics*, 774:395–415, 2015.

[9] J H Lee, Kevin, J P Monty, and N Hutchins. Validating under-resolved turbulence intensities for PIV experiments in canonical wall-bounded turbulence. *Experiments in Fluids*, 57(8):1–11, 2016. ISSN 07234864. doi: 10.1007/s00348-016-2209-6.

[10] Paul Linden. Gravity currents – theory and laboratory experiments. In Eric P Chassignet, Claudia Cenedese, and Jacques Verron, editors, *Buoyancy-driven flows*, chapter 1, pages 13–51. Cambridge University Press, 2012.

[11] Herbert E Huppert. Gravity currents: a personal perspective. *Journal of Fluid Mechanics*, 554:299–322, 2006.

[12] RE Britter and JE Simpson. Experiments on the dynamics of a gravity current head. *Journal of Fluid Mechanics*, 88(2):223–240, 1978.

[13] C. Adduce, G. Sciortino, and S. Proietti. Gravity Currents Produced by Lock Exchanges: Experiments and Simulations with a Two-Layer Shallow-Water Model with Entrainment. *Journal of Hydraulic Engineering*, 138(2):111–121, 2012. ISSN 0733-9429. doi: 10.1061/(ASCE)HY.1943-7900.0000484. URL `http://ascelibrary.org/doi/10.1061/{%}28ASCE{%}29HY.1943-7900.0000484`.

[14] Diana Sher and Andrew W Woods. Gravity currents: entrainment, stratification and self-similarity. *Journal of Fluid Mechanics*, 784:130–162, 2015.

[15] L. Ottolenghi, C. Adduce, R. Inghilesi, F. Roman, and V. Armenio. Mixing in lock-release gravity currents propagating up a slope. *Physics of Fluids*, 28(5), 2016. ISSN 10897666. doi: 10.1063/1.4948760.

[16] Sridhar Balasubramanian and Qiang Zhong. Entrainment and mixing in lock-exchange gravity currents using simultaneous velocity-density measurements. *Physics of Fluids*, 30(5), 2018. ISSN 10897666. doi: 10.1063/1.5023033.

[17] C. S. Yih. *Dynamics of Nonhomogeneous Fluids.* (Macmillan, New York, 1965.

[18] J. E. Simpson and R. E. Britter. The dynamics of the head of a gravity current advancing over a horizontal surface. *Journal of Fluid Mechanics*, 94(3):477–495, 1979.

[19] J E Simpson. Gravity Currents in the Laboratory, Atmosphere, and Ocean. *Annual Review of Fluid Mechanics*, 14(1):213–234, 1982. ISSN 0066-4189. doi: 10.1146/annurev.fl.14.010182.001241. URL `http://www.annualreviews.org/doi/10.1146/annurev.fl.14.010182.001241`.

[20] C Adduce, G Sciortino, and S Proietti. Gravity currents produced by lock exchanges: experiments and simulations with a two-layer shallow-water model with entrainment. *Journal of Hydraulic Engineering*, 138(2):111–121, 2011.

[21] S Balasubramanian and Q Zhong. Entrainment and mixing in lock-exchange gravity currents using simultaneous velocity-density measurements. *Physics of Fluids*, 30 (5):056601, 2018.

[22] Kraig B Winters, Peter N Lombard, James J Riley, and Eric A D'Asaro. Available potential energy and mixing in density-stratified fluids. *Journal of Fluid Mechanics*, 289:115–128, 1995.

[23] WR Peltier and CP Caulfield. Mixing efficiency in stratified shear flows. *Annual review of fluid mechanics*, 35(1):135–167, 2003.

[24] Hesam Salehipour and WR Peltier. Diapycnal diffusivity, turbulent prandtl number and mixing efficiency in boussinesq stratified turbulence. *Journal of Fluid Mechanics*, 775:464–500, 2015.

[25] LD Landau and EM Lifshitz. Fluid mechanics. translated from the russian by jb sykes and wh reid. *Course of Theoretical Physics*, 6, 1987.

[26] Edward N. Lorenz. Available Potential Energy and the Maintenance of the General Circulation. *Tellus*, 7(2):157–167, 1955. ISSN 0040-2826. doi: 10.3402/tellusa.v7i2.8796.

[27] M.C. Gregg, E.A. D'Asaro, J.J. Riley, and E. Kunze. Mixing Efficiency in the Ocean. *Annual Review of Marine Science*, 10(1):443–473, 2018. ISSN 1941-1405. doi: 10.1146/annurev-marine-121916-063643.

[28] TR Osborn. Estimates of the local rate of vertical diffusion from dissipation measurements. *Journal of physical oceanography*, 10(1):83–89, 1980.

[29] GN Ivey and J Imberger. On the nature of turbulence in a stratified fluid. part i: The energetics of mixing. *Journal of Physical Oceanography*, 21(5):650–658, 1991.

[30] J. E. Simpson. Gravity currents in the laboratory, atmosphere, and ocean. *Annual Review of Fluid Mechanics*, 14(1):213–234, 1982.

[31] J Hacker, P. F. Linden, and S. B. Dalziel. Mixing in lock-release gravity currents. *Dynamics of Atmospheres and Oceans*, 24(1-4):183–195, 1996.

[32] Dominik Krug, Markus Holzner, Beat Lüthi, Marc Wolf, Wolfgang Kinzelbach, and Arkady Tsinober. Experimental study of entrainment and interface dynamics in a gravity current. *Experiments in Fluids*, 54(5), 2013. ISSN 07234864. doi: 10.1007/s00348-013-1530-6.

[33] A. T. Fragoso, M. D. Patterson, and J. S. Wettlaufer. Mixing in gravity currents. *Journal of Fluid Mechanics*, 734, 2013.

[34] Q Zhong, F Hussain, and H. J. S. Fernando. Quantification of turbulent mixing in colliding gravity currents. *Journal of Fluid Mechanics*, 851:125–147, 2018.

[35] Peter Pringsheim. Fluorescence and phosphorescence. 1949.

[36] Adrian Ponce, Peter A. Wong, Jeremy J. Way, and Daniel G. Nocera. Intense phosphorescence triggered by alcohols upon formation of a cyclodextrin ternary complex. *Journal of Physical Chemistry*, 97(42):11137–11142, 1993. ISSN 00223654. doi: 10.1021/j100144a040.

[37] Wanda K. Hartmann, Mike H.B. Gray, Adrian Ponce, Daniel G. Nocera, and Peter A. Wong. Substrate induced phosphorescence from cyclodextrin·lumophore host-guest complexes. *Inorganica Chimica Acta*, 243:239–248, 1996. ISSN 00201693. doi: 10.1016/0020-1693(96)04914-6.

[38] C P Gendrich and M M Koochesfahani. A spatial correlation technique for estimating velocity fields using molecular tagging velocimetry (MTV). *Experiments in Fluids*, 22(1):67–77, 1996.

[39] Charles P Gendrich and Manoochehr Koochesfahani. Boundary layer resolved measurements of unsteady leading edge separation on a pitching airfoil. In *APS Division of Fluid Dynamics Meeting Abstracts*, 1998.

[40] B. Stier and M. M. Koochesfahani. Molecular Tagging Velocimetry (MTV) measurements in gas phase flows. *Experiments in Fluids*, 26(4):297–304, 1999. ISSN 07234864. doi: 10.1007/s003480050292.

[41] Ernest M Thurlow and Joseph C Klewicki. Experimental study of turbulent poiseuille–couette flow. *Physics of Fluids*, 12(4):865–875, 2000.

[42] RB Hill and JC Klewicki. Data reduction methods for flow tagging velocity measurements. *Experiments in Fluids*, 20(3):142–152, 1996.

[43] JR Elsnab, D Maynes, JC Klewicki, and TA Ameel. Mean flow structure in high aspect ratio microchannel flows. *Experimental Thermal and Fluid Science*, 34(8): 1077–1088, 2010.

[44] David A Olson, Alan W Katz, Ahmed M Naguib, Manoochehr M Koochesfahani, Donald P Rizzetta, and Miguel R Visbal. On the challenges in experimental characterization of flow separation over airfoils at low reynolds number. *Experiments in fluids*, 54(2):1470, 2013.

[45] Feriel Samouda, Stéphane Colin, Christine Barrot, Lucien Baldas, and Juergen J. Brandner. Micro molecular tagging velocimetry for analysis of gas flows in mini and micro systems. *Microsystem Technologies*, 21(3):527–537, 2013. ISSN 09467076. doi: 10.1007/s00542-013-1971-0.

[46] Hacene Si Hadj Mohand, Aldo Frezzotti, Juergen J. Brandner, Christine Barrot, and Stéphane Colin. Molecular tagging velocimetry by direct phosphorescence in gas microflows: Correction of Taylor dispersion. *Experimental Thermal and Fluid Science*, 83:177–190, 2017. ISSN 08941777. doi: 10.1016/j.expthermflusci.2017.01.002. URL `http://dx.doi.org/10.1016/j.expthermflusci.2017.01.002`.

[47] J. R. Elsnab, J. P. Monty, C. M. White, M. M. Koochesfahani, and J. C. Klewicki. Efficacy of single-component mtv to measure turbulent wall-flow velocity derivative profiles at high resolution. *Experiments in Fluids*, 58(9):128, 2017.

[48] John R. Elsnab, Jason P. Monty, Christopher M. White, Manoochehr M. Koochesfahani, and Joseph C. Klewicki. High-fidelity measurements in channel flow with polymer wall injection. *Journal of Fluid Mechanics*, 859:851–886, 2019. ISSN 14697645. doi: 10.1017/jfm.2018.873.

[49] T Wei, P Fife, J Klewicki, and P McMurtry. Properties of the mean momentum balance in turbulent boundary layer, pipe and channel flows. *Journal of Fluid Mechanics*, 522(2005):303–327, 2005. ISSN 0022-1120. doi: 10.1017/S0022112004001958.

[50] S. L. Thomson and D. Maynes. Spatially Resolved Temperature Measurements in a Liquid Using Laser Induced Phosphorescence. *Journal of Fluids Engineering*, 123(2):293, 2001. ISSN 00982202. doi: 10.1115/1.1365960.

URL http://fluidsengineering.asmedigitalcollection.asme.org/article.aspx?articleid=1429335.

[51] H Hu and M M Koochesfahani. A Novel Technique for Quantitative Temperature Mapping in Liquid by Measuring the Lifetime of Laser Induced Phosphorescence. *Journal of Visualization*, 6(2):143–153, 2003. ISSN 1343-8875. doi: 10.1007/BF03181619.

[52] H. Hu, M. Koochesfahani, C. Lum, J. Coppeta, and C. Rogers. Molecular tagging thermometry with adjustable temperature sensitivity. *Experiments in Fluids*, 40 (5):753–763, 2006. ISSN 07234864. doi: 10.1007/s00348-006-0112-2.

[53] Guillermo J Ferraudi. *Elements of inorganic photochemistry*. Wiley-Interscience, 1988.

[54] Hui Hu and Manoochehr M Koochesfahani. Molecular tagging velocimetry and thermometry and its application to the wake of a heated circular cylinder. *Measurement Science and Technology*, 17(6):1269–1281, 2006. ISSN 0957-0233. doi: 10.1088/0957-0233/17/6/S06.

[55] Mijanur R Chowdhury and Firat Y Testik. A review of gravity currents formed by submerged single-port discharges in inland and coastal waters. *Environmental Fluid Mechanics*, 14(2):265–293, 2014.

[56] Herbert E. Huppert and John E. Simpson. The slumping of gravity currents. *Journal of Fluid Mechanics*, 99(4):785–799, 1980. ISSN 14697645. doi: 10.1017/S0022112080000894.

[57] M Ilıcak. Energetics and mixing efficiency of lock-exchange flow. *Ocean Modelling*, 83:1–10, 2014.

[58] G. O. Hughes and P. F. Linden. Mixing efficiency in run-down gravity currents. *Journal of Fluid Mechanics*, 809:691–704, 2016.

[59] Mehmet Ilicak. Energetics and mixing efficiency of lock-exchange flow. *Ocean Modelling*, 83:1–10, 2015. ISSN 14635003. doi: 10.1016/j.ocemod.2014.08.003.

[60] J Ke and D Bohl. Effect of experimental parameters and image noise on the error levels in simultaneous velocity and temperature measurements using molecular tagging velocimetry/thermometry (MTV/T). *Experiments in Fluids*, 50(2):465–478, 2011. ISSN 07234864. doi: 10.1007/s00348-010-0952-7.

[61] D. G. Bohl. *Experimental study of the 2-D and 3-D structure of a concentrated line vortex array.* Michigan State University. Department of Mechanical Engineering, 2002.

[62] James W. Rottman and John E. Simpson. Gravity currents produced by instantaneous releases of a heavy fluid in a rectangular channel. *Journal of Fluid Mechanics*, 135:95–110, 1983. ISSN 14697645. doi: 10.1017/S0022112083002979.

[63] J. O. Shin, S. B. Dalziel, and P. F. Linden. Gravity currents produced by lock exchange. *Journal of Fluid Mechanics*, 521:1–34, 2004. ISSN 00221120. doi: 10.1017/S002211200400165X.

[64] G. O. Hughes and P. F. Linden. Mixing efficiency in run-down gravity currents. *Journal of Fluid Mechanics*, 809(2016):691–704, 2016. ISSN 14697645. doi: 10.1017/jfm.2016.696.

[65] R W Hyland and A Wexler. Formulations for the thermodynamic properties of the saturated phases of H2O from 173.15 to 473.15 K. *ASHRAE Transaction*, 89: 500–519, 1983.

[66] John D'Errico. Slm-shape language modeling. *SLM-Shape Language Modeling.. http://www. mathworks. com/matlabcentral/fileexchange/24443-slm-shape-language-modeling: Mathworks*, 2009.

[67] T Bonometti and S Balachandar. Effect of schmidt number on the structure and propagation of density currents. *Theoretical and Computational Fluid Dynamics*, 22(5):341, 2008.

[68] Adrien Lefauve, J. L. Partridge, Qi Zhou, S. B. Dalziel, C. P. Caulfield, and P. F. Linden. The structure and origin of confined Holmboe waves. *Journal of Fluid Mechanics*, 848:508–544, 2018. ISSN 14697645. doi: 10.1017/jfm.2018.324.

[69] A Wexler and R. W. Hyland. A formulation for the thermodynamic properties of the saturated pure ordinary water-substance from 173.15 to 473.15 k. *Final report, ASHREA Research Project PR*, 216:1980, 1980.

[70] Dominik Krug, Daniel Chung, Jimmy Philip, and Ivan Marusic. Global and local aspects of entrainment in temporal plumes. *Journal of Fluid Mechanics*, 812:222–250, 2017.

[71] D. A. Hebert and S. M. de Bruyn Kops. Relationship between vertical shear rate and kinetic energy dissipation rate in stably stratified flows. *Geophysical research letters*, 33(6), 2006.

[72] A. T. Fragoso, M. D. Patterson, and J. S. Wettlaufer. Mixing in gravity currents. *Journal of Fluid Mechanics*, 734:1–10, 2013. ISSN 00221120. doi: 10.1017/jfm.2013.475.

[73] R B Dean. Reynolds Number Dependence of Skin Friction and Other Bulk Flow Variables in Two-Dimensional Rectangular Duct Flow. *Journal of fluids engineering*, 100(June 1978):215–223, 1978.

[74] J. P. Monty and M. S. Chong. Turbulent channel flow: Comparison of streamwise velocity data from experiments and direct numerical simulation. *Journal of Fluid Mechanics*, 633:461–474, 2009. ISSN 00221120. doi: 10.1017/S0022112009007769.

[75] A Nagashima. Viscosity of water substance—New international formulation and its background. *Journal of Physical and Chemical Reference Data*, 6(4):1133–1166, 1977.

Author/s:
Agrawal, Tanmay

Title:
Investigation of mixing in gravity currents using high-resolution molecular tagging techniques

Date:
2020

Persistent Link:
http://hdl.handle.net/11343/267792

File Description:
Final thesis file